

TABLE 1.  
 Fraction of Color and Morphology-selected Objects

$I$	Full Sample	Color Selected	FWHM Selected	Combined Selection	Color/ Full	Combined/ Color	Combined/ Full
M31 Halo Field							
17-18	144	102	75	55	0.71	0.54	0.38
18-19	192	136	89	64	0.71	0.47	0.33
19-20	237	130	104	66	0.55	0.51	0.28
20-21	430	223	176	101	0.52	0.45	0.23
21-22	805	379	314	184	0.47	0.49	0.23
22-23	1384	629	592	333	0.45	0.53	0.24
23-24	2156	992	1069	543	0.46	0.55	0.25
24-25	1996	1052	1103	620	0.53	0.59	0.31
(Matched) Comparison Field							
17-18	64	47	37	30	0.73	0.64	0.47
18-19	109	54	53	33	0.50	0.61	0.30
19-20	211	105	72	50	0.50	0.48	0.24
20-21	298	127	103	65	0.43	0.51	0.22
21-22	488	189	149	75	0.39	0.40	0.15
22-23	837	275	326	116	0.33	0.42	0.14
23-24	1262	373	594	186	0.30	0.50	0.15
24-25	880	287	442	135	0.33	0.47	0.15

TABLE 2.  
Observed Star Counts and EGM Predictions

Field	Area [arcmin <sup>2</sup> ]	$X^a$ [kpc]	$Y^a$ [kpc]	Observed		EGM Predictions <sup>b</sup>	
				$I=20-22$	$I=22-24$	$I=20-22$	$I=22-24$
This Study	210.0	-1.7	-18.7	122 <sup>c</sup>	543 <sup>c</sup>	421 (421)	6141 (6140)
G302 <sup>d</sup>	3.3	-2.5	-6.7	339	1756	132 (119)	1955 (1748)
G312 <sup>d</sup>	3.3	+0.5	-11.1	82	436	33 (32)	486 (479)
G1 <sup>e</sup>	1.1	+33.6	+4.6	33	140	10 (6)	157 (91)

<sup>a</sup> ( $X$ ,  $Y$ ) = Projected distance of field center from M31's center along its major and minor axes, respectively

<sup>b</sup> Numbers in parentheses indicate spheroid stars

<sup>c</sup> The star selection efficiency for our  $R = 19$  kpc sample is estimated to be about 30% for the brighter apparent magnitude range and probably as low as 10%–20% for fainter stars

<sup>d</sup> From the study by Holland et al. (1996)

<sup>e</sup> From the study by Rich et al. (1996)

# Isolating Red Giant Stars in M31's Elusive Outer Spheroid

David B. Reitzel and Puragra Guhathakurta<sup>1</sup>

UCO/Lick Observatory, University of California, Santa Cruz, California 95064, USA

Electronic mail: reitzel@ucolick.org, raja@ucolick.org

Andrew Gould<sup>1</sup>

Department of Astronomy, Ohio State University, 174 West 18th Avenue,  
Columbus, Ohio 43210-1106, USA

Electronic mail: gould@astronomy.ohio-state.edu

## ABSTRACT

Deep *UBRI* images of a  $15' \times 15'$  field in the outer spheroid of the M31 galaxy obtained using the Kitt Peak National Observatory 4-meter telescope, and *I* band images obtained with the Keck 10-meter telescope and Low Resolution Imaging Spectrograph, are used to isolate a sample of candidate red giant branch stars located at a projected radial distance of 19 kpc along the minor axis. These stars are distinguished from the more numerous distant field galaxies on the basis of broadband  $U - B$ ,  $B - R$ , and  $R - I$  colors and image morphology: We isolate objects whose colors are consistent with the long, but relatively narrow locus occupied by red giants in *UBRI* color space (as observed in Galactic globular cluster giants and predicted by models spanning a wide range of metallicities and ages), and those whose angular sizes are consistent with the stellar point spread function,  $\text{FWHM} = 0''.6 - 0''.9$  (Keck) and  $\text{FWHM} = 0''.9 - 1''.5$  (Kitt Peak). We carry out the same analysis of data on a comparison field with a similar Galactic latitude to the M31 halo field. The color-magnitude diagram of objects in the comparison field is well described by a superposition of foreground Galactic dwarf stars (in keeping with a standard empirical model of the Galaxy) against a backdrop of contaminating faint blue field galaxies ( $I \gtrsim 21$ ,  $B - I \sim 1 - 2.5$ ), while the M31 halo field contains a clear excess of faint red objects ( $I \sim 20 - 23$ ,  $B - I \sim 2 - 3.5$ ) in addition to these two components. The location of this population of faint red objects in the color-magnitude diagram is as would be expected for red giant stars at the distance of M31. The surface density of red giant candidates in the  $R = 19$  kpc M31 halo field is

---

<sup>1</sup>Alfred P. Sloan Research Fellow

consistent with the findings of two recent *Hubble Space Telescope* studies. The data indicate that M31’s stellar halo is much denser and/or larger than that of the Galaxy:  $(\rho_{\text{M31}}^{\text{RGB}}/\rho_{\text{MW}}^{\text{RGB}})(\Lambda/1.5)^{-\nu} \sim 10$ , where  $\Lambda$  is the ratio of the radial scale lengths of M31 and the Galaxy and  $\nu = -3.8$  is the assumed power law index of the density profile; in fact, M31’s profile may be steeper than this ( $\nu < -3.8$ ). The color and slope of the red giant branch in M31’s outer halo are suggestive of a relatively metal-rich population,  $[\text{Fe}/\text{H}] \gtrsim -1$ , in agreement with the *Hubble Space Telescope* measurements.

*Subject headings:* galaxies: individual: Andromeda galaxy [Messier 31 (M31), NGC 224, UGC 454, CGCG 535-017] – galaxies: formation – stars: red giants – stars: metallicity

## 1. Introduction

Studying the metallicity gradient of galactic spheroids is crucial for understanding their formation and evolutionary history. The dissipational collapse model (Eggen et al. 1962; Larson 1974) predicts a strong metallicity gradient because of progressive chemical enrichment during the collapse of the protogalactic gas cloud. The accretion model (Searle & Zinn 1978), on the other hand, predicts no strong gradient because star formation largely precedes assembly of the galactic spheroid. The metallicity gradient of a halo can be measured in both the globular cluster system and in field stars; in fact, it is important to study both populations independently since they may be dynamically distinct from each other.

Globular clusters are easily observed out to large distances in the Galaxy because of their high luminosity and this allows a reliable determination of the metallicity gradient in the system of Galactic globular clusters. Zinn (1993) finds evidence for two subsystems among clusters: an ‘old halo’ population which displays a radial  $[\text{Fe}/\text{H}]$  gradient, a small age spread, and significant rotation, and a ‘young halo’ population which displays no metallicity gradient, a large age spread, and very little rotation. He associates the former population with the initial dissipational collapse of the Galactic halo (a la Eggen et al. 1962) and the latter with subsequent accretion of stellar systems (a la Searle & Zinn 1978). On the other hand, Carney et al. (1990) find a mean metallicity of  $[\text{Fe}/\text{H}] = -1.72$  and an absence of a strong metallicity gradient as a function of apogalacticon distance over the range  $8 \text{ kpc} \leq R_{\text{apo}} \leq 40 \text{ kpc}$  in a proper motion selected survey of 227 Galactic field halo stars with velocities lagging the local standard of rest’s circular velocity by at least  $150 \text{ km s}^{-1}$ .

It seems logical to test the universality of the conclusions about galaxy formation which are being drawn from the single case of the Galaxy. The Andromeda galaxy (M31) provides an external perspective of a large spiral similar to our own and yet is close enough for individual stars to be resolved. Huchra et al. (1991) showed that there is evidence for a weak metallicity gradient in a sample of 150 M31 globular clusters, with a mean metallicity of  $[\text{Fe}/\text{H}] = -1.2$ , which is slightly higher than the mean value of  $[\text{Fe}/\text{H}] = -1.4$  for Galactic globular clusters.

Over the last decade, several groups have tried to determine the metallicity of field red giant branch (RGB) stars in M31’s spheroid, starting with the early work of Crots (1986). Mould & Kristian (1986) found a metallicity of  $[\text{Fe}/\text{H}] = -0.6$  for stars in a field located at a projected distance of  $R = 7$  kpc along the minor axis, and assumed that the observed color spread was due to a large metallicity dispersion. Mould (1986) failed to determine the metallicity at  $R = 20$  kpc, because the contaminating field galaxies could not be removed by the standard method of morphological selection and statistical subtraction. Pritchett & van den Bergh (1988) estimated  $[\text{Fe}/\text{H}] = -1.0$  at  $R = 8.6$  kpc on the minor axis, and again attributed the large color spread to an intrinsic spread in  $[\text{Fe}/\text{H}]$ . Christian & Heasley’s (1991) data in an  $R = 16$  kpc field around the globular cluster G219 suggested a large metallicity spread, with a mean value  $[\text{Fe}/\text{H}] \gtrsim -1.0$ , as did Davidge’s (1993) study at  $R = 6.7$  kpc, Durrell et al.’s (1994) study, and Couture et al.’s (1995) study which targeted fields around five M31 globular clusters. While these studies have furthered our knowledge of M31’s halo, sample contamination by distant field galaxies, foreground Galactic dwarfs, and M31 disk giants poses a serious obstacle in attempts to determine the metallicity of M31’s outer halo ( $R \gtrsim 10$  kpc).

Two recent studies of the M31 spheroid have taken advantage of the excellent angular resolution of *Hubble Space Telescope* (*HST*) Wide Field/Planetary Camera 2 images to separate stars from distant field galaxies. In the first study, Rich et al. (1996) analyze archival *HST* images of a field centered on the M31 globular cluster G1. The line of sight to this field (Fig. 1) intersects M31’s highly inclined disk ( $i \sim 77^\circ$ ; de Vaucouleurs 1958) at a relatively large radius  $R_{\text{disk}} \approx R = 40$  kpc on the major axis (the value of  $R_{\text{disk}}$  could be different if M31’s outer disk is warped). The second study is that of Holland et al. (1996) who analyze deep *HST* images of two fields around M31 globular clusters located 7.6 kpc (G302) and 10.8 kpc (G312) from the center roughly along the SE minor axis (Fig. 1). Both studies find the mean metallicity of M31’s halo RGB stars to be comparable to that of 47 Tuc ( $[\text{Fe}/\text{H}] = -0.7$ ), with a spread of nearly 2 dex, suggesting that there was a greater degree of pre-enrichment during the assembly of M31’s spheroid than in the case of the Galaxy’s spheroid. We will return to a more detailed discussion of these studies later in the paper (Sec. 4.2).

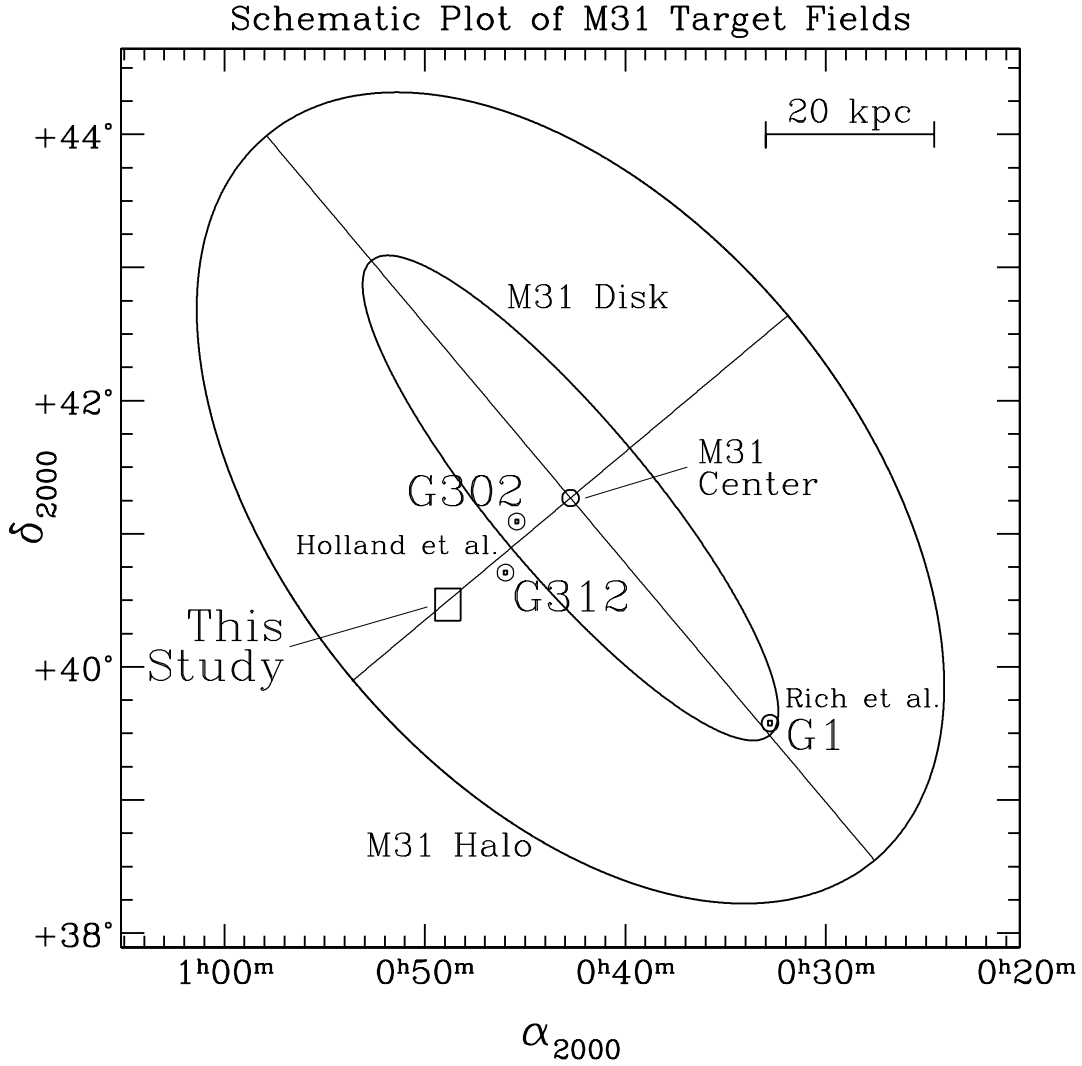


Fig. 1.— Schematic plot showing the approximate location of the field studied in this paper, along with Holland et al.’s (1996) G302 and G312 fields and Rich et al.’s (1996) G1 field. The size of each square symbol marking field position corresponds to the actual area of the field studied, but not to the field shape. The ellipses indicate the orientation of M31’s disk ( $i = 77^{\circ}$ ,  $\text{PA} = 40^{\circ}$ , with finite thickness) and halo (5:3 flattening, same PA as disk); the sizes of the ellipses are arbitrary. The 10% change in the  $\cos(\delta)$  projection factor from the top to the bottom of the plot has been ignored in this schematic representation.

In this paper, we probe RGB stars in the M31 halo using an alternative method for discriminating between stars and faint galaxies; one that uses a combination of broadband *UBRI* colors and morphological information (Gould et al. 1992, hereafter referred to as GGRF). Early results have been reported by Reitzel et al. (1996a,b). The field of study presented here is at a projected distance of  $R = 19$  kpc from M31’s center along the minor axis (only Rich et al.’s G1 field is at a comparable radial distance out in the spheroid assuming it has a 5:3 flattening) and the line of sight to the field intersects M31’s disk at  $R_{\text{disk}} \approx 75$  kpc, further out than in any of the previous studies (Fig. 1). The area of the field in this study,  $210 \text{ arcmin}^2$ , is more than 60 times larger than each of the Holland et al. fields, and more than 40 times larger than the Rich et al. G1 field. Moreover, the field stars targeted in this study are well away from any of M31’s globular clusters. The observations and data reduction procedure are described in Sec. 2. The technique used to isolate M31 halo RGB stars from background field galaxies and foreground Galactic dwarfs is described in Sec. 3. In Sec. 4, we discuss the properties of M31’s spheroid in the context of the recent *HST* studies and outline plans for future work. The main points of the paper are summarized in Sec. 5.

## 2. The Data

### 2.1. Observations

We present observations of an outer spheroid field in M31 and a comparison field carried out with the the Kitt Peak National Observatory (KPNO) 4-meter telescope and a  $2048 \times 2048$  Tektronix CCD during 4 nights in November 1993. The M31 halo field:

$$\alpha_{J2000} (\text{M31 halo}) = 00^{\text{h}}48^{\text{m}}51^{\text{s}}.0; \quad \delta_{J2000} (\text{M31 halo}) = +40^{\circ}28'05'' \quad (1)$$

is located  $84'$  from the galaxy’s center, at a projected radial distance of 18.8 kpc for an assumed distance modulus of  $(m - M)_0 = 24.43$  mag or  $D = 770$  kpc (Freedman & Madore 1990), at a position angle of  $124.8^{\circ}$  (E of N) putting it close to M31’s SE minor axis (Fig. 1); the position angle of the M31 disk major axis is  $40^{\circ}$ . The comparison field:

$$\alpha_{J2000} (\text{Comp}) = 07^{\text{h}}49^{\text{m}}00^{\text{s}}.0; \quad \delta_{J2000} (\text{Comp}) = +60^{\circ}03'46'' \quad (2)$$

provides a control sample: its Galactic coordinates [ $l^{\text{II}}(\text{Comp}) = 157^{\circ}$ ,  $b^{\text{II}}(\text{Comp}) = +30^{\circ}$ ] are roughly similar to those of the M31 halo field [ $l^{\text{II}}(\text{M31 halo}) = 122^{\circ}$ ,  $b^{\text{II}}(\text{M31 halo}) = -22^{\circ}$ ]. We compare the number, magnitude distribution, and color

distribution of Galactic stars in the two fields in the context of the Bahcall & Soneira (1984) model (see Sec. 3.4 for details).

The data set consists of images through  $U$ ,  $B_J$ ,  $R$ , and  $I$  filters with bandpasses centered at 3600, 4500, 6500, and 9000 Å, respectively. Note, this bandpass system is roughly similar, but *not* identical, to the standard Johnson/Kron/Cousins bandpass system. The pixel scale is  $0''.47$  and the field of view of each individual CCD frame is  $16' \times 16'$ . The FWHM of the seeing disk ranges from  $0''.9 - 1''.5$  across the data set, and is generally smallest for  $I$  band exposures. The primary observations consist of short (15 min in  $U$ , 10 min in each of  $B_JRI$ ), slightly disregistered exposures of the M31 halo field: a total of 21 exposures in  $U$ , 14 in  $B_J$ , 13 in  $R$ , and 14 in  $I$  corresponding to effective total exposure times of 5.3 hr in  $U$  and 2.2 – 2.3 hr in each of  $B_JRI$ . The total exposure times are somewhat shorter for the comparison field: 15 exposures in  $U$  (3.8 hr), 11 in  $B_J$  (1.8 hr), 8 in  $R$  (1.3 hr), and 9 in  $I$  (1.5 hr).

In order to empirically verify the locus of RGB stars in multicolor space, we use short  $UB_JRI$  exposures of 6 Galactic globular clusters spanning a range of metallicities. The data for the clusters M15, M79, and M2 are of adequate depth and quality; we are unable to use the data for the other 3 clusters, NGC 7006, NGC 6934, and Pal 11, as the surface density of cluster giants is too low relative to contaminating field Galactic dwarfs. Short  $UB_JRI$  exposures of standard star fields (Landolt 1983) are used for photometric calibration of the data. The globular cluster and standard star exposures are from two photometric nights during the observing run. In addition, a sequence of zero-second bias frames and short  $I$  band twilight flat exposures are used for data processing.

For the purpose of measuring angular sizes of faint objects, we use  $I$  band images of the M31 halo field obtained using the Keck 10-meter telescope and the Low Resolution Imaging Spectrograph (LRIS, Oke et al. 1995) during 1 night in September 1995. The 4 Keck/LRIS exposures,  $1 \times 10$  min and  $3 \times 5$  min, form a (mostly) non-overlapping  $2 \times 2$  mosaic covering about 75% of the field of view of the KPNO image. The scale of the Keck images is  $0''.22 \text{ pixel}^{-1}$  and the field of view of each CCD frame is  $5'.7 \times 7'.3$ . The FWHM of seeing is  $0''.6 - 0''.9$  for the Keck observations. Limited use is made of these Keck data; unless specifically mentioned, all subsequent data references in the paper pertain to the main KPNO data set.



## 2.2. Flat Fielding, Fringe Removal, & Coaddition of the Data

Each CCD image is overscan subtracted, trimmed, and bias subtracted in the usual way. The  $U$ ,  $B_J$ , and  $R$  images are then flat fielded using “dark sky flats”. Each dark sky flat is the median combination, with  $\pm 2\sigma$  rejection of cosmic rays, stars, and galaxies, of all the disregistered images in that band of both M31 halo and comparison fields (20–35 images per filter). The  $I$  band images are flat fielded differently from those in  $UB_JR$  as the raw CCD frames in  $I$  contain Fabry-Perot fringing of night sky emission lines. An  $I$  band flat field image is created by median combining twilight flat exposures with  $\pm 2\sigma$  rejection; these images are dominated by the (solar) continuum and are largely free of fringing. All  $I$  exposures are first flat fielded with the twilight flat, which corrects for spatial variation of quantum efficiency across the CCD but leaves the fringe pattern intact. A fringe template is created by median combining the twilight-flat-fielded  $I$  exposures of the M31 halo and comparison fields with  $\pm 2\sigma$  rejection, and by reducing the resulting image to zero mean. The amplitude of the fringe pattern is found to vary from image to image (roughly 0.5%–1.5% of the sky level), so the fringe template is scaled individually to optimize fringe removal for each  $I$  band image.

The images are geometrically transformed to correct for slight image distortion ( $\lesssim 10^{-3}$ ) and aligned for coaddition. Each image is scaled to correct for any variation in transparency as a function of airmass and/or time (typically  $\lesssim 10\%$ ), as determined from measurements of secondary photometric standard stars on the image. An additive offset is then applied to match the sky background level over common areas of all images in a given band, correcting for time variations in the night sky brightness (most extreme in the  $I$  band). The transparency- and background-matched images in each band are median combined with  $\pm 2\sigma$  rejection of cosmic rays. Cosmic rays are then masked from each image by comparing the image to the median image in that bandpass. Finally, all images in a given band ( $UB_JRI$ ) are averaged, excluding masked pixels. The combined images each cover an area of about  $15' \times 15'$ ; the dithering between exposures slightly reduces the overlap area compared to the field of view of individual CCD frames.

## 2.3. Artifact Correction

The combined CCD images suffer from two kinds of artifacts in the vicinity of bright stars ( $B \lesssim 17$ ,  $I \lesssim 15$ ): charge bleeding and amplifier hysteresis. These problems are most severe in the  $I$  band image (as the brightest stars are quite red in color and because the instrumental throughput is highest in this band) and least in the  $U$  band image. While the artifacts cover only a small fraction of the total image area ( $\sim 1\%$ ), they hamper the

performance of the automated object detection and photometry software over a larger surrounding area. We apply a set of techniques that reduce, but do not eliminate, the effect of artifacts in the M31 halo field image. We do not correct artifacts in the comparison field as it is less severely affected than the M31 halo field (higher Galactic latitude, and hence fewer bright stars). The affected areas of the comparison field ( $\approx 6\%$  of its area), and the artifact-corrected M31 halo field ( $\approx 8\%$  of its area) are properly accounted for in the subsequent analysis (Sec. 2.5).

Extreme saturation of pixels near the center of the image of a bright star can lead to the overflow of charge along CCD columns ( $y$  axis). We interpolate the sky background row by row across the affected region by fitting a linear function in  $x$  with a  $\pm 2\sigma$  rejection to avoid stars/galaxies. While this procedure obviously does not recover any of the data in the pixels occupied by the bleed, it replaces each bleed with a smoothly varying background, thereby allowing faint objects to be detected in the neighborhood of bright stars.

Amplifier hysteresis results in a temporary change in the effective gain immediately after reading out saturated pixels ( $\sim 1\%$  decrease in  $R$  and  $I$ ,  $\lesssim 10\%$  increase in  $B$  and  $U$ ), with the gain gradually returning to its nominal level. This produces prominent streaks of low or high values extending for several hundred pixels ( $2' - 6'$ ) along the  $x$  axis to the right of all bright stars (i.e., downstream in the readout sequence). Multiple streaks caused by the numerous bright stars in the M31 halo field combine to form an uneven background and affect the probability of faint object detection. Each of these streaks is rectified as follows: (1) A linear function in  $x$ ,  $f_{\text{ref}}(x)$ , is fit to a 10 pixel-wide (in  $y$ ) reference region above and below the streak, extending along the full length of the streak in  $x$ , with  $\pm 2\sigma$  rejection of stars/galaxies; (2) A linear function in  $x$ ,  $f_i(x)$ , is similarly fit to each row  $i$  of the streak; and (3) The difference,  $f_{\text{ref}}(x) - f_i(x)$ , is added to each row ( $i$ ) of pixels in the streak. This technique does an excellent job of correcting for amplifier hysteresis while preserving: (a) the intensity distribution of a star or galaxy whose image happens to lie, partly or wholly, within a streak and (b) possible large scale gradients in the sky background level.

## 2.4. Detection and Photometry of Stars and Galaxies

After rectifying charge bleed and amplifier hysteresis artifacts in the data, we construct a single deep image for each of the M31 halo and comparison fields. This image is constructed from the weighted sum of the images in all 4 bands. The weights are chosen to maximize the signal-to-noise ratio for a faint object whose  $UB_JRI$  colors are roughly equal to those of a typical faint RGB star. The software package FOCAS (Jarvis & Tyson 1981; Valdes 1982) is used to analyze the M31 halo field and comparison field data in the

following way: (1) A catalog of individual objects (stars and galaxies) is derived from the deep, summed  $U+B_J+R+I$  image using a matched filter search technique (with search parameters tuned to maximize faint object detection efficiency while minimizing the fraction of spurious detections), and a limiting isophote is defined for each object; and (2) For each star/galaxy, this limiting isophote is applied to the image in each of the 4 bands ( $UB_JRI$ ) to obtain photometry—i.e., color measurements are based on these “common optimized apertures”. We have checked that, for a set of relatively isolated objects, the `FOCAS` apparent magnitude agrees to within  $\lesssim 0.03$  mag with the “total” apparent magnitude derived from a standard curve of growth analysis.

After accounting for the difference in line-of-sight reddening between the M31 halo and comparison fields,  $E(B - V) = 0.085$  and  $0.038$ , respectively (Burstein & Heiles 1982), we find a small offset between the  $UBRI$  loci of bright (foreground) stars between the two fields corresponding to a residual magnitude zeropoint difference in the  $B$  band. This difference is probably caused by errors in the transparency correction; empirical checks indicate that the difference is not likely to be a result of PSF differences or errors in the assumed  $E(B - V)$ . We apply a slight adjustment to the  $B$  magnitude scales of both data sets (0.1 mag) to bring them into agreement with each other and with the theoretical Bertelli et al. (1994)  $UBRI$  stellar loci (Sec. 3.2). This zeropoint adjustment does not affect any of the conclusions in this paper—the intrinsic widths of the color selection regions are  $\gtrsim 0.1$  mag (Fig. 4) and all magnitude measurements are assumed to have an associated systematic error of  $\pm 0.1$  mag in the data analysis (Sec. 2.5).

We have carried out tests using three different photometry techniques: `FOCAS`, aperture photometry with curve of growth corrections, and PSF-fitting using the digital stellar photometry program `DAOPHOT` (Stetson 1987, 1992). The results obtained from these techniques are not vastly different. The `FOCAS` limiting isophotes are better matched to the light distribution of galaxies of widely varying shapes and sizes than fixed apertures and suffer less from contamination in crowded fields. The `FOCAS` “common optimized aperture” color measurements are somewhat more robust than the `DAOPHOT` measurements for the resolved galaxies in the data set; the two techniques yield comparable results for unresolved objects.

The Galactic globular cluster images are analyzed with the help of the `DAOPHOT` applying the `FIND` and `ALLSTAR` tasks in the usual way. We use a linearly variable point spread function (PSF) template to account for slight distortion in image quality across the image. Position-dependent aperture corrections are applied to convert the apparent magnitudes returned by `ALLSTAR` to total magnitudes.

The `FOCAS`-based (M31 halo and comparison fields) and `DAOPHOT`-based (Galactic

globular clusters) total instrumental magnitudes are transformed to the standard Johnson/Kron/Cousins *UBRI* system as defined by the set of Landolt (1983) photometric standards. The transformation parameters in each band, derived from observations of standard star fields, include a zeropoint accurate to  $\lesssim 0.05$  mag, a shutter time constant of 0.07 s (same for all bands), an independent airmass coefficient for each of the two photometric nights, and a linear (Johnson/Kron/Cousins) color term. The color term, particularly large for the  $B_J^{\text{instr}} \rightarrow B^{\text{Johnson}}$  conversion, is applied iteratively starting with the instrumental color as an initial guess. We hereafter use the term “*UBRI* magnitudes” to refer to calibrated magnitudes on the Johnson/Kron/Cousins system (Landolt 1983).

## 2.5. Photometric Accuracy and Completeness

We estimate the photometric error associated with the measurement of *UBRI* magnitudes of stars/galaxies in the M31 halo and comparison fields. In the M31 halo field, the Poisson error is 0.05 mag for objects with  $U = 23.0$ ,  $B = 24.1$ ,  $R = 23.3$ , and  $I = 22.6$ , and increases to 0.25 mag for objects with  $U = 25.5$ ,  $B = 26.7$ ,  $R = 25.9$ , and  $I = 25.1$ . These estimates are based on shot noise in the photons detected from the object, and on the area of the limiting *FOCAS* isophote and the shot noise per pixel in the sky counts. The overall error in the final calibrated magnitude is likely to be somewhat larger than the Poisson error because of the following: flat-fielding error, residual image artifacts, error in measuring the value of the local sky background, neighbor contamination (varying degrees of contamination among the 4 bands can lead to color errors), unaccounted for light outside limiting isophote (this does not affect color measurements to first order), and calibration error. An empirical check of the measured *UBRI* colors of Galactic dwarf stars in the M31 halo and comparison fields shows that they agree with the Bertelli et al. (1994) model predictions to within  $\sim \pm 0.05$  mag; nevertheless, we conservatively assume that these other sources of error contribute an additional (systematic) uncertainty of 0.1 mag (over Poisson error) in all magnitude measurements (see Sec. 3.2).

Based on the sky noise level in the final M31 halo field images, we compute  $3\sigma$  limiting apparent magnitudes within an aperture of area 28.3 pixels or  $6.25 \text{ arcsec}^2$  (this is roughly equal to the minimum allowable isophotal area in the *FOCAS* object detection algorithm):  $U_{\text{lim}} = 25.6$ ,  $B_{\text{lim}} = 26.7$ ,  $R_{\text{lim}} = 25.7$ , and  $I_{\text{lim}} = 25.0$ . Note, these limiting magnitudes are based on a *fixed* aperture size, whereas the error estimates in the previous paragraph are based on the *actual* isophotal area of each object. The remainder of the data analysis presented in this paper is restricted to the sample of stars/galaxies that satisfy the criteria:  $B < B_{\text{lim}}$ ,  $R < R_{\text{lim}}$ , and  $I < I_{\text{lim}}$ . As discussed in Sec. 3.2 below, the *U* band is the most

critical of the 4 bands in discriminating between faint galaxies and red giants, even in cases where there is only an upper limit to the apparent  $U$  brightness of an object. We have therefore chosen *not* to impose the  $U$  limiting magnitude criterion in defining the sample. Instead, any object whose measured  $U$  brightness falls formally below the threshold is treated as a non-detection in the  $U$  band, and is assigned a well-defined upper limit to its brightness,  $U > U_{\text{lim}}$ , for the purpose of color selection (Sec. 3.2).

Even after applying the above cuts in apparent  $BRI$  magnitude, the sample of stars and galaxies detected in the M31 halo and comparison fields is not complete over all regions of the CCD image: FOCAS’s object detection routine has difficulty finding objects in areas of the  $U + B + R + I$  image surrounding very bright galaxies and stars, especially those with charge bleed artifacts. The nominal area covered by the M31 halo data set (field of view of KPNO image) is about  $227 \text{ arcmin}^2$  but a fraction of this area,  $(1 - P_0) = 0.08$ , is effectively lost. Even though  $P_0$  is probably a weak function of apparent magnitude, it is adequate for our purposes to assume it is a constant. We estimate  $P_0$  by comparing the total number of objects detected down to the completeness limits over the entire KPNO image to the *expected* total number based on the observed surface density of objects over the same magnitude range in “clean” areas of the image (i.e., areas free of very bright stars/galaxies, charge bleeds, and hysteresis artifacts).

Since the majority of faint objects in the M31 halo field are distant field galaxies (an isotropic population), we can estimate the degree of completeness of the sample by comparing the observed counts,  $N(m)$ , to counts of a statistically complete sample of galaxies derived from the high-quality, Hubble Deep Field (HDF) data set (Williams et al. 1996). For the purpose of this comparison only, the above limiting magnitude criteria are ignored and the entire KPNO data set is used. The *HST* instrumental magnitudes of HDF galaxies are converted to the Johnson/Kron/Cousins  $UBRI$  magnitude system adopted in this paper using the transformation relations given by Holtzman et al. (1995); the observed distribution of galaxies in the  $B - R$  vs  $B - I$  plane (in both M31 halo and comparison fields) is used to interpolate each HDF galaxy’s  $R$  band magnitude. For the 4 bands, the apparent magnitude at which the completeness drops to half the maximum value is:  $U_{50} = 26.3$ ,  $B_{50} = 27.6$ ,  $R_{50} = 26.5$ , and  $I_{50} = 25.8$ . These values are significantly fainter than the  $3\sigma$  limiting apparent magnitudes at which the data set is truncated; the completeness fraction is essentially 100% for objects brighter than the limiting magnitudes.

## 2.6. Angular Size Measurements

The angular diameter ( $\theta_{\text{FWHM}}$ ) of each object detected in the M31 halo field and comparison field is measured using the final, coadded KPNO  $I$  band images, as they have the best seeing of the 4 bands (FWHM of seeing is about  $1''.2$  and  $1''.5$  in the two fields, respectively). The seeing in a few of the individual 10 min KPNO  $I$  exposures is as good as  $0''.8$  (FWHM), but these images do not have adequate signal-to-noise for the majority of the objects which are quite faint. For each object,  $\theta_{\text{FWHM}}$  is determined by fitting a Gaussian to the azimuthally-averaged radial intensity profile. The outer parts of the stellar PSF are not very well described by a Gaussian so the  $\theta_{\text{FWHM}}$  values reported in this paper may be systematically different from measurements based on a more realistic PSF template; this study however relies only on the *relative* angular sizes of objects (Sec. 3.3).

We also determine widths of the best fit Gaussian profiles for objects that lie in the area of the M31 halo field covered by the Keck/LRIS  $I$  band images. The Keck data set has better angular resolution ( $0''.6 - 0''.9$  seeing FWHM and  $0''.22 \text{ pixel}^{-1}$  scale) than the coadded KPNO image and is of comparable or greater depth (the factor of 6 larger primary mirror area and better seeing more than compensate for the much shorter exposure times). We use Keck-based  $\theta_{\text{FWHM}}$  measurements in preference to those derived from the KPNO data whenever available; the former allow improved morphological distinction between stars and compact galaxies at faint apparent magnitudes.

## 3. Searching for M31 Halo Red Giants: Needles in a Haystack

### 3.1. Defining the Stellar Locus in $UBRI$ space

Accurate definition of the loci of RGB stars in  $UBRI$  space is very important for the color selection technique used in this paper. Following the method used by GGRF who determined stellar loci using the Yale stellar evolution models (Green et al. 1987), we determine RGB stellar loci using the Bertelli et al. (1994) stellar evolution models. The Bertelli et al. model isochrones match the color distribution of Landolt (1983) standard stars extremely well, in the Johnson/Kron/Cousins  $UBVRI$  photometric system defined by these stars. Since the photometric calibration of the KPNO data set used in this paper is tied to these same Landolt standards (in terms of magnitude zeropoints and color transformations), the Bertelli et al. models are a natural choice for defining the stellar loci used in this study.

We use Bertelli et al. model isochrones bracketing the 5 – 20 Gyr range of ages and

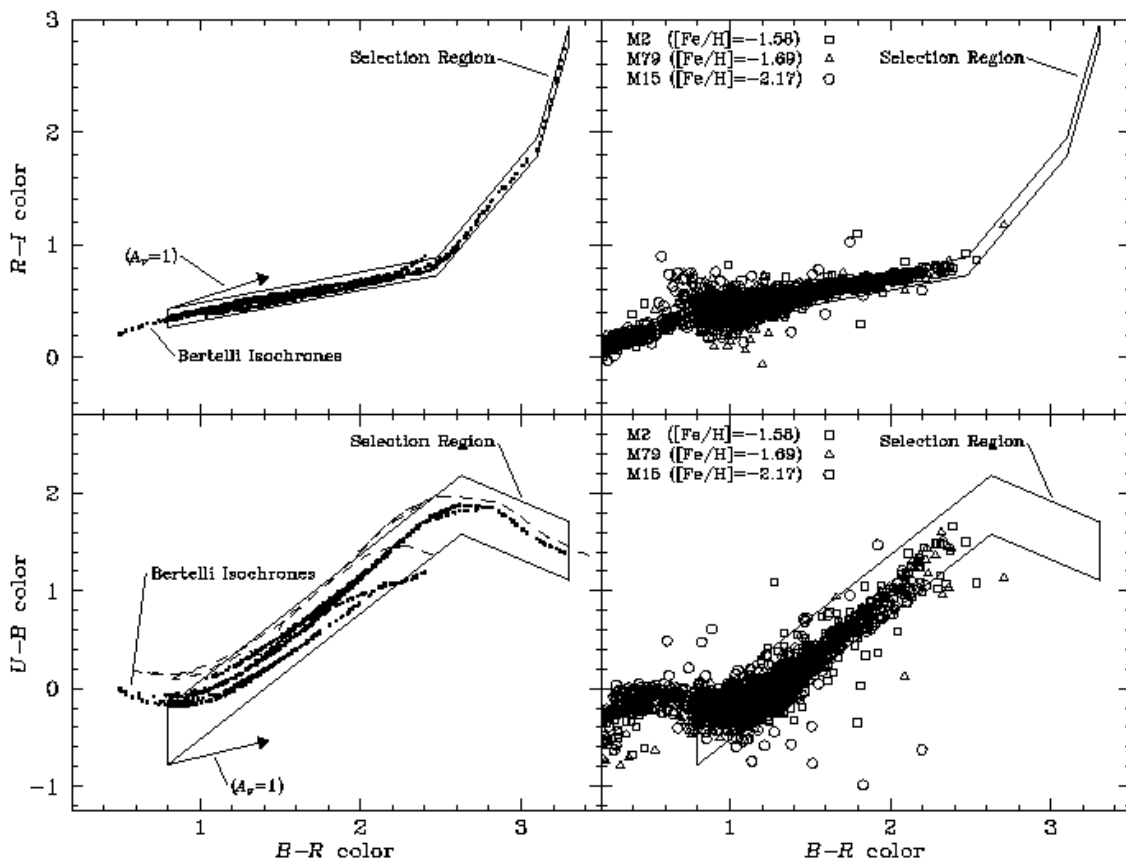


Fig. 2.— The loci of stars in the  $BRI$  and  $UBR$  color-color diagrams. [All colors are adjusted to the amount of reddening appropriate for the M31 halo field,  $E(B - V) = 0.085$ .] *Left panels*—Theoretical isochrones from Bertelli et al. (1994) for ages of 5 – 20 Gyr and for metallicities of  $[\text{Fe}/\text{H}] = -1.70$  to  $[\text{Fe}/\text{H}] = 0$  (bold dots). The dashed line in the lower left panel corresponds to a 1 Gyr stellar population with super-solar metallicity,  $[\text{Fe}/\text{H}] = +0.4$ . The isochrones exclude main sequence stars with  $M \lesssim 0.6 M_{\odot}$  causing an artificial truncation (e.g., at  $B - R = 2.4$ , isochrones  $U - B = 1.2$ ). The solid lines define the “selection parallelogram”, the region used to select RGB stars in the M31 halo and comparison fields. The reddening vector is shown for  $A_V = 1$  mag (its location in the color-color plane is arbitrary). *Right panels*—Distribution of relatively metal poor stars in the Galactic globular clusters, M2 (squares), M79 (triangles), and M15 (circles), along with the RGB selection regions shown in the left panels. The distribution of cluster RGB stars is in good agreement with theoretical models; the feature extending beyond the blue end of the selection region ( $B - R < 0.8$ ) is formed by cluster horizontal branch stars.

for the metallicity range  $[\text{Fe}/\text{H}] = -1.70$  to  $[\text{Fe}/\text{H}] = 0$  (bold dots in left panels of Fig. 2) to define the stellar selection loci in the  $R - I$  vs  $B - R$  and  $U - B$  vs  $B - R$  color-color planes. The isochrones are reddened by an amount appropriate for the M31 halo field,  $E(B - V) = 0.085$  (Burstein & Heiles 1982), using a standard Galactic interstellar dust extinction law (Cardelli et al. 1989). The selection region (the narrow region in Fig. 2 with parallel sides which we refer to as a “parallelogram” for simplicity) is defined as the region that completely encompasses all of the RGB points in the isochrones. While we do not expect there to be many young or high metallicity objects, we have chosen the selection region to avoid biasing the resulting sample to any particular metallicity or age.

Even though the stellar locus is very extended in any one color (e.g., it spans the range  $0.8 < B - R < 3.3$ ), the different colors are strongly correlated and this makes the locus narrow in color-color space. Changes in metallicity and age tend to move stars mostly along the length of the stellar loci: this is especially true in the  $BRI$  color-color diagram; increasing  $[\text{Fe}/\text{H}]$  does make the  $U - B$  color slightly redder at fixed  $B - R$ , so the width of the  $UBR$  color-color selection region is correspondingly wider to account for this.

We perform two independent empirical checks to verify the accuracy of the stellar locus definitions and the photometric conversion of instrumental magnitudes to the Johnson/Kron/Cousins system:

- (1) Globular cluster data, obtained in the same  $UB_JRI$  system in conjunction with the M31 halo field and comparison field observations, yield a distribution of RGB stars that is in good agreement with the Bertelli et al. (1994) model isochrones. This is shown in the right panels of Fig. 2 (the sequence of stars beyond the left edge of the selection box corresponds to the cluster horizontal branch). Prior to the comparison, the colors of the globular cluster stars are dereddened and then adjusted to the line-of-sight reddening estimated for the M31 halo field,  $E(B - V) = 0.085$  (Burstein & Heiles 1982). Note however that data are only available for the relatively metal-poor clusters, M15, M2, and M79, thereby restricting the check to the range:  $-2.5 \lesssim [\text{Fe}/\text{H}] \lesssim -1.5$ .
- (2) As discussed in Sec. 3.2 below, the distribution of foreground Galactic metal-rich ( $[\text{Fe}/\text{H}] \sim 0$ ) disk dwarf stars in  $UBRI$  color-color diagrams of the M31 halo and comparison fields is consistent with Bertelli et al. isochrones of solar or super-solar metallicity (compare dashed line in lower left panel of Fig. 2 to lower left panel of Fig. 3). This check is indirect however because the foreground stars are (mostly) main sequence stars whereas the selection loci are optimized for red giants.



### 3.2. Color Selection

The main source of contamination for the study of M31’s faint spheroid stars is the population of background faint field galaxies. These galaxies are expected to be about as common as M31 halo stars at faint magnitudes (there are 25 arcmin<sup>-2</sup> down to  $B = 26$ ) and a fair fraction have small angular sizes, which makes it difficult to distinguish them from stars on the basis of image morphology alone. The expected surface density of M31 spheroid red giants in this 19 kpc field is less than 26 arcmin<sup>-2</sup> down to  $I = 24$  ( $B \sim 26$ ) as discussed in Sec. 4.2. GGRF have developed a method which uses accurate *UBRI* CCD photometry for isolating faint stars ( $B < 26$ ) and rejects most of the background galaxies on the basis of colors while eliminating only a fraction of the stars. The essence of the method lies in the fact that stars occupy a relatively tight locus in any color-color diagram (Fig. 2), while galaxies exhibit a broad distribution of colors.

Figure 3 demonstrates the basis for the color selection method via *BRI* and *UBR* color-color plots of all objects detected in the M31 halo field. For an object to appear in these color-color plots and in the  $\Delta U$  vs  $\Delta I$  color excess plots below (Fig. 4) it must satisfy the  $U < U_{\text{lim}}$  criterion along with the usual *BRI* criteria; this additional restriction causes there to be substantially fewer objects in these plots than in the full sample (cf. Figs. 6 and 7), especially at the faint end of the distribution. The left panels include all objects brighter than the expected tip of the M31 RGB,  $I < 20.5$ . Most of the bright objects in this low latitude ( $|b| = 22^\circ$ ) M31 halo field are foreground Galactic stars as evidenced from the fact that they lie close to the defined selection region. The selection regions are, however, optimized for red giant stars of solar or lower metallicity, while most of these bright objects are disk dwarfs with high (possibly super-solar) metallicity. Thus it is not surprising that the  $I < 20.5$  objects deviate from the selection region slightly, especially in the *UBR* diagram. The right panels of Fig. 3 show all objects with  $I > 20.5$ , which includes any M31 RGB stars as well as a large number of distant field galaxies. It is obvious that the galaxies occupy a more extensive region of the plot than do the stars. In the *BRI* diagram, the galaxies are slightly redder in  $R - I$  ( $\sim 0.4$  mag) than the stellar locus at a given  $B - R$  color; the separation is clearer in the *UBR* diagram: for example, the typical galaxy is  $\gtrsim 1$  mag bluer in  $U - B$  than the stellar locus for  $B - R \gtrsim 2$ .

Following GGRF we use each object’s measured  $B - R$  color and the stellar locus to predict the colors,  $(R - I)_{\text{pred}}$  and  $(U - B)_{\text{pred}}$ , an RGB star would have if it had the same  $B - R$  color as the object. The measured colors of the object are then used to calculate color excesses:

$$\Delta I = -[(R - I) - (R - I)_{\text{pred}}] \tag{3}$$

$$\Delta U = (U - B) - (U - B)_{\text{pred}} \quad (4)$$

The color excesses measure the vertical distance in the  $BRI$  and  $UBR$  color-color diagrams of each object from center line of the stellar locus “parallelogram” (Fig. 2). The  $U$  data are pivotal in the application of the color selection technique to red giants, even though the low intrinsic stellar brightness and relative inefficiency of the instrument in the ultraviolet conspire to make  $U$  band detection of distant RGB stars a challenging prospect. As described in Sec. 2.5, objects that are fainter than the limiting magnitude in  $U$  (but which satisfy the apparent brightness criteria in  $BRI$ ) are assigned a  $U$  band color excess  $\Delta U > \Delta U_{\text{lim}}$ , where  $\Delta U_{\text{lim}} = (U_{\text{lim}} - B) - (U - B)_{\text{pred}}$ .

Figure 4 shows the distribution of color excesses. The relatively bright objects ( $17 < I < 20.5$ ) in the M31 halo field shown in the left panel lie near but not exactly at the origin. This is only to be expected: while most of these bright objects are foreground Galactic stars, they are main sequence stars and not red giants. In the center and right panels, we plot the fainter objects ( $20.5 < I < 25$ ) in the M31 halo and comparison fields, respectively. Note the broad and asymmetric distribution of these faint objects in  $(\Delta I, \Delta U)$  space most of which belong to the faint background field galaxy population (especially in the comparison field, right panel).

Color selection is accomplished by requiring objects to have colors consistent with both  $BRI$  and  $UBR$  stellar loci. An object is considered to pass color selection only if its color excesses  $(\Delta I, \Delta U)$  are such that the  $1.5\sigma$  measurement error ellipse intersects a rectangular reference region centered on the origin (Fig. 4), where the width and height of the rectangle are equal to the vertical width of the “parallelogram” selection regions in the  $BRI$  and  $UBR$  color-color plots, respectively (Fig. 2). In other words, an object is assigned a color-based classification of “star-like” only if  $\delta < 1.5$ , where  $\delta$  is the *significance*, in units of the photometric error, of the separation of the object from the point closest to it within the central rectangular area in  $(\Delta I, \Delta U)$  space. Like GGRF, we determine the measurement errors for  $\Delta I$  and  $\Delta U$  jointly, as there is a strong covariance between these quantities. For each  $U$  band non-detection that is brighter than the limiting magnitudes in  $BRI$ , we check whether the combination of its  $\Delta I$  value and  $\Delta U > \Delta U_{\text{lim}}$  criterion is consistent with the rectangle at the origin.

### 3.3. Morphological Selection

The  $UBRI$  color selection described above yields a sample of objects consisting of M31 RGB stars, foreground Galactic stars (mostly disk dwarfs), and any field galaxies whose

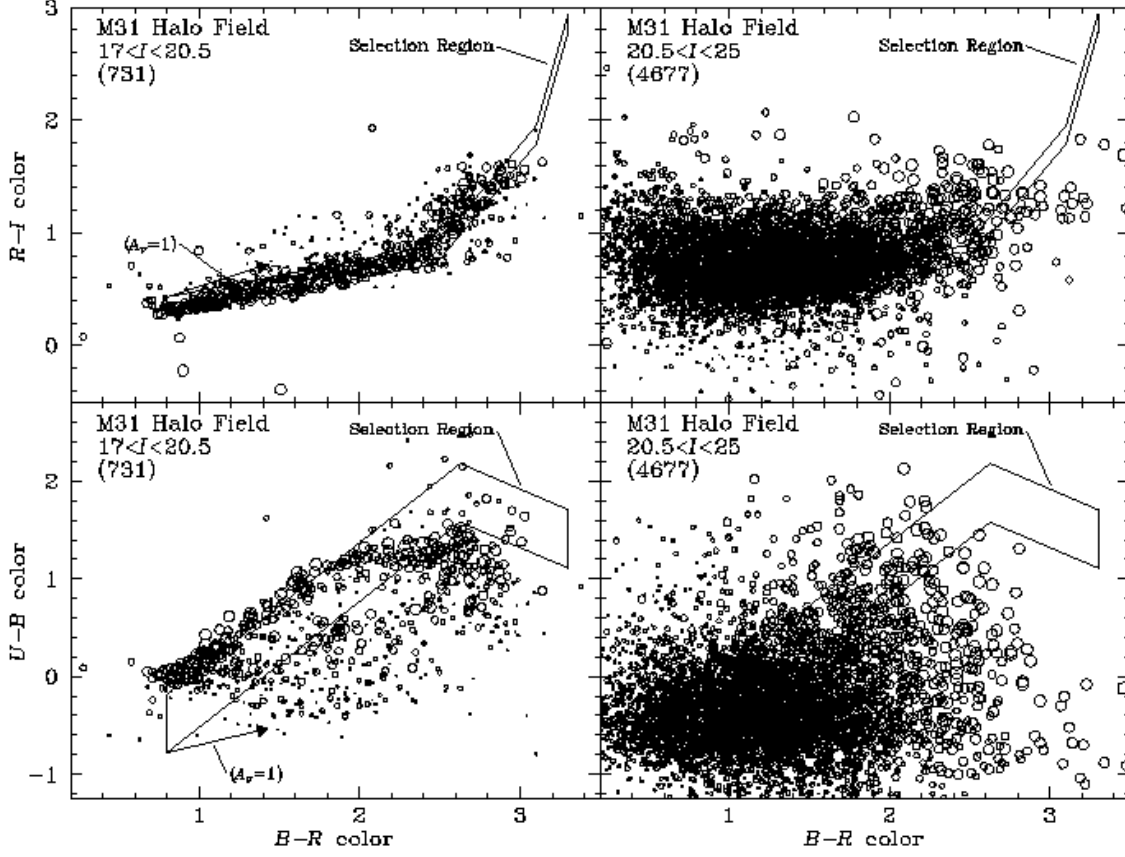


Fig. 3.— Color-color diagrams for the M31 halo field:  $R - I$  vs  $B - R$  (upper panels) and  $U - B$  vs  $B - R$  (lower panels). Point size is scaled with apparent  $I$  magnitude, with larger dots indicating brighter objects. The left panels show objects with  $17 < I < 20.5$ . These bright objects are mostly foreground main sequence stars in the Galactic disk; their distribution matches the selection region (see dashed line in Fig. 2), though not perfectly as selection is optimized for lower metallicity RGB stars. The right panels show objects with  $20.5 < I < 25$ . The majority of the objects in this faint magnitude range are galaxies which have a much larger spread in color than the stars. Note, most galaxies with  $B - R \gtrsim 2$  are  $\sim 1$  mag bluer in  $U - B$  than the selection region.

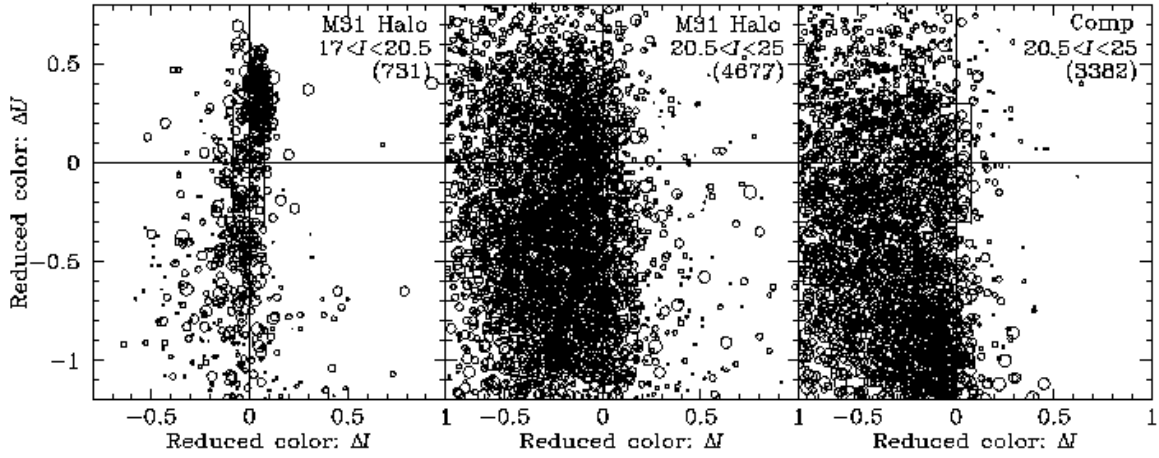


Fig. 4.— The distribution of color excess indices,  $\Delta I$  and  $\Delta U$ . Dot size scales with apparent  $I$  magnitude: large dots = bright objects, and vice versa. The left panel shows objects with  $17 < I < 20.5$  in the M31 halo field: most of these are Galactic dwarfs with high metallicities, with colors that deviate slightly from the expected locus of RGB colors. The center and right panels show objects with  $20.5 < I < 25$  in the M31 halo field and the comparison field, respectively; the majority of these are faint galaxies (especially in the comparison field) exhibiting a broad distribution of color excesses. The width and height of the bold rectangle at the origin correspond to the vertical widths of the selection regions used in the  $BRI$  and  $UBR$  planes, respectively.

colors happen to be consistent with stellar loci. We also apply the more traditional method of star-galaxy separation based on image morphology.

Figure 5 shows the distribution of angular sizes ( $\theta_{\text{FWHM}}$ ) of objects in the M31 halo field as measured on the KPNO image and on one of the Keck/LRIS *I* band images. About half the objects in the sample are well resolved relative to the stellar PSF,  $\theta_{\text{FWHM}} > \theta_{\text{crit}}$  (morphologically “galaxy-like”); the rest are assigned a morphological classification of “star-like”. We adopt  $\theta_{\text{crit}} = 1''.36$  for the KPNO image, and  $\theta_{\text{crit}} = 0''.73, 0''.84, 0''.86,$  and  $0''.88$  for the 4 Keck/LRIS images. These  $\theta_{\text{crit}}$  values are slightly larger than the FWHM of the PSF in the center of the corresponding CCD image to allow for variations in the PSF across the field of view: the stellar image quality is degraded near the corners of the field due to optical distortion/focus variation. For an object larger than a few arcseconds, the measured size is typically inaccurate since it is based on a Gaussian fit. This does not affect our analysis, however, since  $\theta_{\text{FWHM}}$  for such objects is invariably large; hence the objects are correctly classified as morphologically galaxy-like.

Keck/LRIS-based star-galaxy separation is used in preference to KPNO-based star-galaxy separation in areas where both measurements are available (75% of the M31 halo field); the superior angular resolution and signal-to-noise ratio of the Keck *I*-band data result in improved star-galaxy discrimination, especially in the case of compact, barely resolved galaxies and blended groups of faint objects. It is possible to compare star-galaxy discrimination based on Keck vs KPNO  $\theta_{\text{FWHM}}$  measurements in the area where the two data sets overlap: the morphological classification is star-like by both methods for 34% of the objects, galaxy-like by both methods for 26%, star-like according to the Keck measurement and galaxy-like according to the KPNO measurement for 27%, and vice versa for 13%.

The distribution of measured angular sizes may be used to investigate whether the color selection technique is working. In the unselected sample, 56.0% of all objects with  $I \leq 20$  have  $\theta_{\text{FWHM}}$  values that lead to their being classified as morphologically star-like, whereas after color selection 61.6% of the objects are morphologically star-like. For  $I \leq 23$ , only 44.4% of all objects have stellar profiles, yet 53.4% of the color selected objects are star-like. For  $I \leq 25$ , 48.8% of the full (non-color selected) sample has star-like morphology, compared to 55.3% for the color selected sample. The fact that the fraction of morphologically star-like objects is higher in the color selected sample than in the full sample is indicative that color selection is indeed picking out stars. The effect is subtle since neither morphological selection nor color selection alone is perfectly efficient. A fraction of the stars ( $\sim 30\%$ ) happen to be scattered beyond  $\delta > 1.5$  due to photometric error, and there are compact galaxies that fail the *UBRI* selection criterion as well as

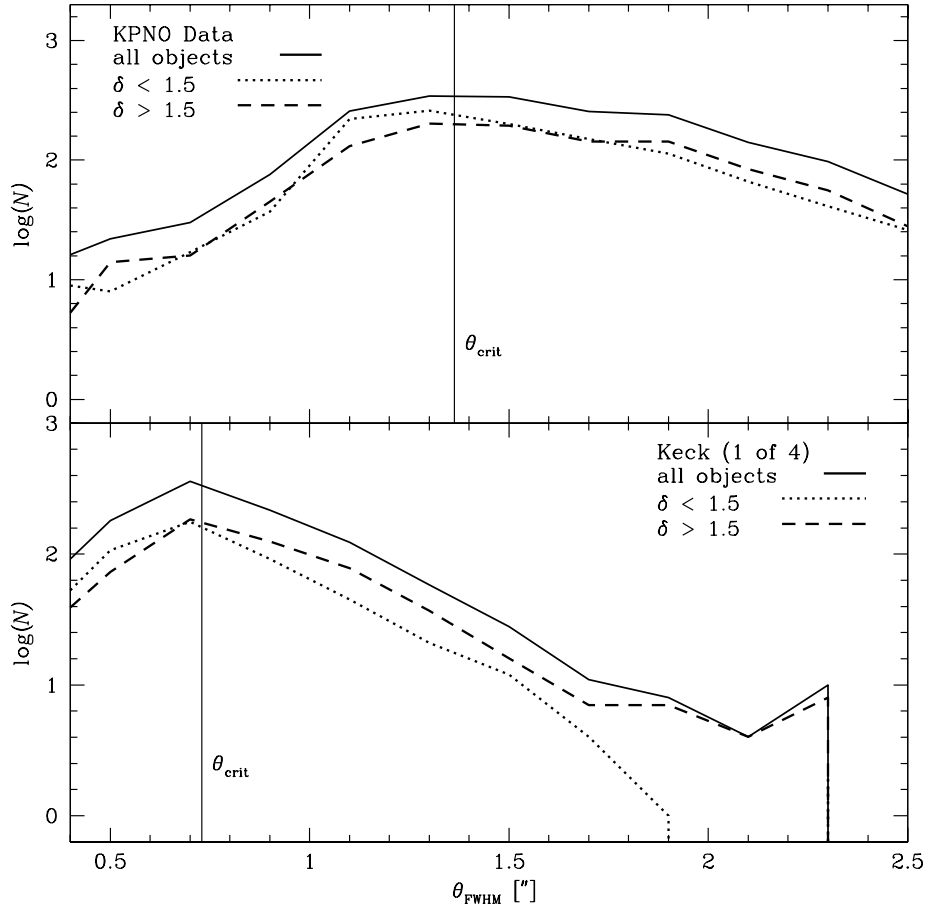


Fig. 5.— The distribution of angular sizes for objects detected in the M31 halo field as measured on the KPNO image (upper panel) and on one of the four Keck images (lower panel). The threshold for morphological selection,  $\theta_{\text{crit}}$ , is indicated by a vertical line. The solid curve shows the entire (unselected) sample; the dotted curve is for objects whose colors are consistent with those of an RGB star ( $\delta < 1.5$ ), while the dashed curve is for the rest of the objects ( $\delta > 1.5$ ). Note, objects with  $\delta < 1.5$  tend to be more compact than those with  $\delta > 1.5$ , an indication that the color selection does preferentially select stars.

extended galaxies whose colors happen to intersect the RGB locus. Furthermore, errors in the measurement of angular size (due to object/sky photon noise, neighbor contamination, etc.) cause  $\theta_{\text{FWHM}}$  for some stars to scatter beyond  $\theta_{\text{crit}}$ , especially at faint magnitudes.

There is nothing special about our use of  $\theta_{\text{FWHM}}$  measurements for star-galaxy discrimination nor about our particular choices of  $\theta_{\text{crit}}$  values. After carrying out tests of FOCAS’s Bayesian star-galaxy separation scheme on the data sets, we choose to adopt the simpler  $\theta_{\text{FWHM}}$  measurement scheme; the effect of noise on star-galaxy discrimination is easier to quantify in the latter scheme. It is worth noting however that results based on the FOCAS morphological classification are not qualitatively different from those based on  $\theta_{\text{FWHM}}$  measurements. The  $\theta_{\text{FWHM}}$ -selected sample no doubt includes some compact galaxies for which the measured angular size is less than the critical value. Conversely, a small fraction of stars are scattered across to  $\theta_{\text{FWHM}} > \theta_{\text{crit}}$  due to measurement error in the angular size caused by noise and/or the presence of neighbors. We have chosen  $\theta_{\text{crit}}$  values to achieve a balance between contamination vs incompleteness.

### 3.4. Detection of Red Giants in M31

The detection of M31 RGB stars against the numerous background field galaxies and foreground Galactic stars is difficult, but the combined power of color and FWHM selection yields a sample of M31 halo RGB stars. The pre-selection color-magnitude diagram (CMD) of all objects detected in the M31 halo field is shown in Fig. 6(a); it is practically impossible to see any concentration of M31 RGB stars in this plot. After FWHM selection a hint of concentration of M31 RGB stars becomes visible in the CMD [Fig. 6(b)]. Morphological selection removes 51.2% of the objects in the full sample, most of them relatively well resolved galaxies, yet contamination from compact galaxies and foreground main sequence stars remains. The *UBRI* selection technique removes 49.7% of the full set of objects [Fig. 6(c)]. Most foreground lower main sequence stars with  $B - I > 3$  are removed (these deviate systematically from the RGB loci) as are a significant fraction of the distant field galaxies (these have a broad distribution in color-color space), yet galaxies whose *UBRI* colors happen to be close to those of a RGB star survive selection. While a concentration of M31 RGB stars in the CMD is again revealed, as for the FWHM selected sample, the exact location of the concentration is uncertain due to contamination. When FWHM and color selection are applied simultaneously, the complimentary nature of these selection screens reveals a fairly clean sample of M31 RGB stars [Fig. 6(d)]. Comparing the Galactic globular cluster RGB fiducials of M5 and 47 Tuc [plotted in Fig. 6(b) and (c), but not in (d) so as not to guide the reader’s eye] to the main concentration in the FWHM- and

*UBRI*-selected CMD [Fig. 6(d)], it is clear that the objects detected are in a location of the CMD appropriate for M31 RGB stars.

We carry out a detailed comparison between the M31 halo field sample and the sample of objects found in the comparison field. The final image of the comparison field has an area of 254 arcmin<sup>2</sup>; its effective area is 94.1% of this, or 239 arcmin<sup>2</sup> ( $P_0$  has been estimated in the same way as for the M31 halo field—see Sec. 2.5). The M31 halo field has a smaller effective area (88%) than the comparison field. The latter data set is scaled down in order to match the effective area of the M31 halo field by removing a random 12% of the objects from the sample. This reduces the number of objects in the full (unselected) comparison field sample to 4217. The matched comparison field data set is then processed through the same *UBRI* color selection and FWHM selection screens as the M31 halo field data set. The comparison field data were obtained under slightly worse seeing conditions than the M31 halo field data; the KPNO *I* band comparison field data set is used for morphological selection with  $\theta_{\text{crit}} = 1''.65$ . No Keck/LRIS images of the comparison field are available for FWHM measurements.

Figure 7 shows *I* vs  $B - I$  CMDs of the M31 halo and comparison fields (upper and lower panels, respectively), clearly demonstrating the presence of an additional component of red giants in the former data set. The left panels [(a) and (b)] contain the full data sets prior to any selection. Even in this non-selected sample, it is obvious that the M31 halo field contains many more objects than the comparison field, 7469 versus 4217. This is mostly due to the additional population of M31 RGB stars, although as we discuss below, the M31 halo field does contain a larger number of foreground Galactic stars since it is at a somewhat lower Galactic latitude. In the center panels [(c) and (d)] we compare the fields after *UBRI* selection: 50.3% of the M31 halo field objects survive, while only 36.1% of the comparison field objects survive, an indication of the larger population of objects with star-like colors in the former field. The additional population of M31 RGB stars is plainly visible, even though many galaxies with star-like colors remain. The right panels [(e) and (f)] contain only objects that have both star-like colors and morphology. There is a noticeable additional component of M31 halo stars in Fig. 7(e). As much as 57.0% of the FWHM selected M31 halo field objects survive the additional color selection, while only 41.1% survive in the comparison field.

The objects that survive color and morphological selection in the comparison field [Fig. 7(f)] represent a mix of Galactic stars and compact galaxies that happen to have star-like colors. RGB fiducials for the Galactic globular clusters M5 and 47 Tuc are also plotted to indicate the region of the CMD where M31 RGB stars are expected to be concentrated. The significant concentration of additional objects in the M31 halo field



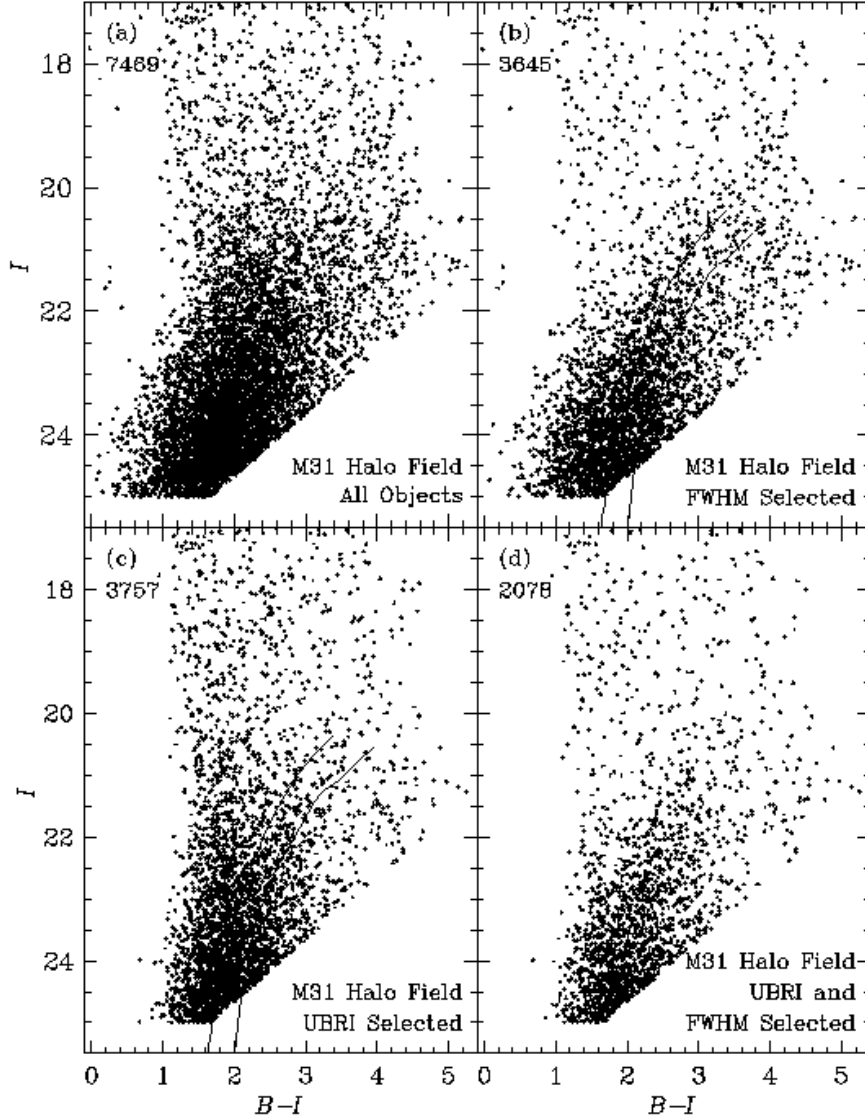


Fig. 6.— (a) Color-magnitude diagram of all M31 halo field objects. (b) CMD after morphological selection. (c) CMD after  $UBRI$  color selection. (d) CMD after  $UBRI$  and FWHM selection. The number of objects in each panel is indicated in the upper left. Most of the bright objects ( $I \lesssim 20$ ) are foreground Galactic stars, the prominent vertical edge at  $B - I = 1$  representing the main sequence turnoff, while the majority of faint objects are distant galaxies. The diagonal concentration of faint red objects that survive in (d) resembles the RGB fiducials of Galactic globular clusters displaced to  $D_{M31} = 770$  kpc shown in (b) and (c): [L→R] M5 ( $[Fe/H] = -1.4$ ) and 47 Tuc ( $[Fe/H] = -0.70$ ).

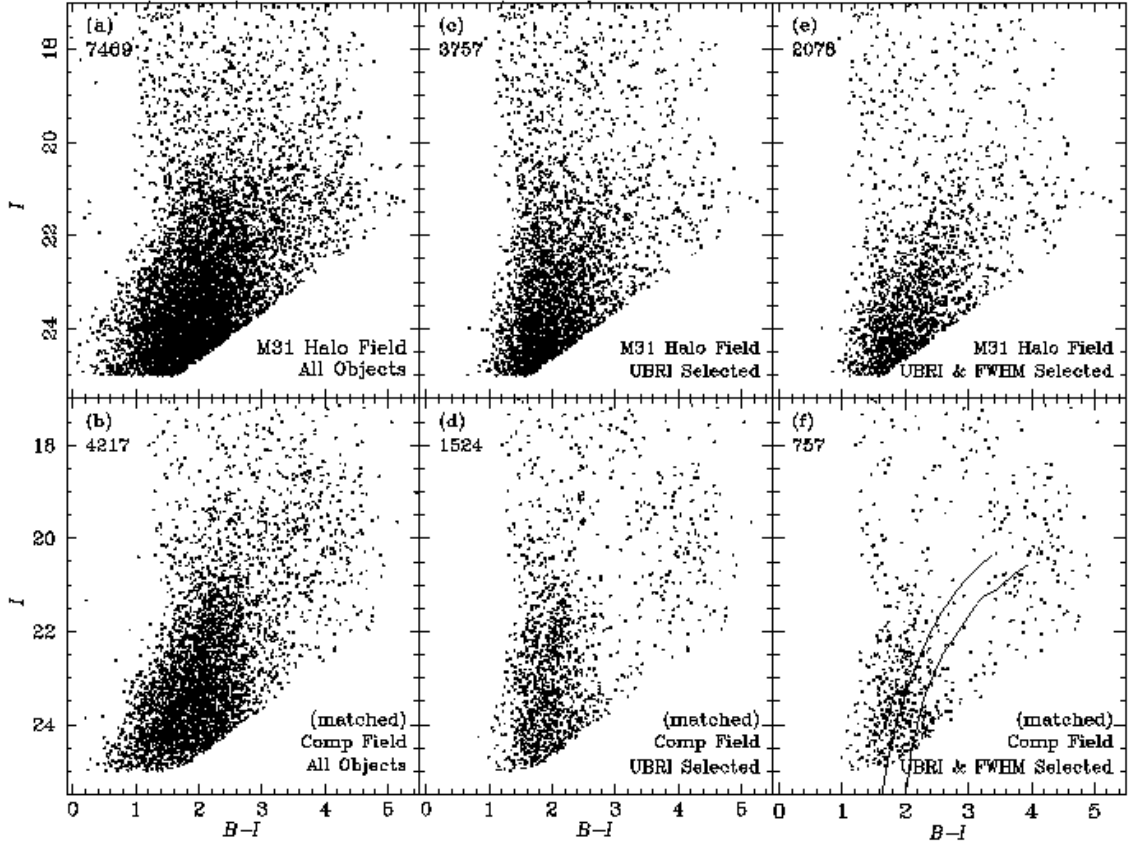


Fig. 7.— (a+b) Color-magnitude diagrams of all objects in the M31 halo and comparison fields, respectively, with the latter scaled down to correct for the difference in the effective areas of the two data sets. (c+d) Same as (a+b) after *UBRI* selection. (e+f) Same as (a+b) after *UBRI* and morphological selection. The number of objects in each panel is indicated in the upper left. The unselected M31 halo field contains many more objects than the corresponding comparison field sample but it is difficult to identify the additional population in the former sample [compare (a) vs (b)]. Note the significant concentration in (e) of additional objects (RGB stars) in the final *UBRI*- and FWHM-selected M31 halo field data set. This may be compared to the RGB fiducials of M5 and 47 Tuc plotted in (f), as for Fig. 6.

sample [Fig. 7(e)] is indeed at this expected CMD location; the M31 halo field also contains the foreground and background populations that are present in the comparison field CMD. The *UBRI*- and FWHM-selected M31 halo field sample contains 1321 more objects than the corresponding comparison field sample. The number of these additional M31 halo field objects increases towards fainter apparent *I* magnitudes (see Table 1). There are 145 additional objects in the range  $20 < I < 22$ , and 574 additional objects in the range  $22 < I < 24$ . Even in the magnitude range brighter than the expected tip of the M31 RGB,  $I < 20$ , there are 116 more objects in the M31 halo field than in the comparison field. This is due to the higher surface density of foreground Galactic stars in the M31 halo field.

The degree of foreground contamination due to Galactic stars in the M31 halo and comparison fields is investigated using an empirical model of the Galaxy (IASG model—Ratnatunga & Bahcall 1985). The model incorporates standard density profile parameters and metallicity distributions for the Galaxy’s spheroid, thin disk, and thick disk to compute the predicted stellar color and apparent magnitude distributions. These model CMDs are compared to the CMDs of the M31 halo and comparison fields. While the IASG model has not been tested at faint magnitudes, the bright end stellar distributions agree well with the M31 halo and comparison field data [Figs. 8(a), (b), (c), and (d)]. Note the “wall” of main sequence turnoff stars near the left edge of each panel. The predicted density of stars with  $I < 20$  and  $B - I < 3.5$  agrees with that observed in the corresponding fields. The IASG model seems to over predict the number of stars with  $B - I > 3.5$ ; in fact, recent star count analyses by Gould et al. (1996, 1997) indicate that the abundance of low luminosity red ( $B - I > 3.5$ ) main sequence stars in the Galaxy is lower by a factor of  $\sim 3$  than that predicted by the IASG model. Another reason for the discrepancy between the M31 halo CMD and the IASG model CMD [Figs. 8(a) vs (c)] is that many of these faint red stars are screened out of the M31 halo sample during *UBRI* selection because the locus of such stars departs from the RGB locus on which the selection “parallelogram” is based (see left panels of Figs. 2 and 3).

### 3.5. Statistical Removal of Contaminants from M31 RGB Sample

We use the color- and morphology-selected, area-matched comparison field data set [Fig. 8(b)] to assess the amount of contamination in the corresponding M31 halo field sample. Each object in the comparison field CMD is matched to the object “closest” to it in color-magnitude location in the scaled M31 halo CMD, provided it is located within a local elliptical region. This elliptical region is arbitrarily defined by semi axes lengths of 0.3 mag in  $B - I$  color and 0.5 mag in apparent *I* magnitude. The matched pairs are removed

from both CMDs. Only 81 objects remain unmatched out of the 757 in the *UBRI*- and FWHM-selected comparison field sample ( $\sim 10\%$ ), while 1402 out of 2078 (67%) remain unmatched in the scaled M31 halo field. This preliminary sample of “excess” objects in the M31 halo field shows a strong concentration around the expected CMD location of RGB stars at the distance of M31 [Fig. 8(e)]:  $\text{CMD}_{8e} = \text{CMD}_{8a} - \text{CMD}_{8b}$ .

The M31 halo field is closer to the Galactic plane ( $|b| = 22^\circ$ ) than the comparison field ( $|b| = 30^\circ$ ), and is expected to contain 1.7 times more foreground Galactic dwarf stars than the area matched comparison field sample on the basis of the IASG model [compare Figs. 8(c) and (d)]. We carry out another statistical subtraction between the two IASG model CMDs to estimate the number and distribution in color-magnitude space of the *extra* foreground Galactic stars in the scaled M31 halo field. We also simulate the fall off in *UBRI* selection efficiency for low luminosity, red main sequence stars by excluding an increasing fraction of stars with  $B - I > 3.5$ ; the excluded stars are indicated by crosses in Figs. 8(c) and (d). This sample of extra IASG model stars is then used to (statistically) remove *residual* foreground contaminants from the preliminary statistically-subtracted M31 halo field sample to obtain the final sample of M31 halo RGB candidates [Fig. 8(f)]:  $\text{CMD}_{8f} = \text{CMD}_{8e} - (\text{CMD}_{8c} - \text{CMD}_{8d})$ .

### 3.6. Star Selection Efficiency

The efficiency of the *UBRI*- and FWHM-based star selection procedure may be estimated by studying the fraction of objects selected at every step of the procedure, coupled with *a priori* knowledge of the ratio of stars to galaxies, as a function of apparent brightness. Table 1 shows the selected numbers and fractions of objects for both M31 halo and comparison fields in 1 mag bins in the *I* band. At bright magnitudes ( $I < 19$ ), the surface density of field galaxies is only 0.43 arcmin<sup>2</sup> (Lilly et al. 1995a,b) or about 90 galaxies in the KPNO field, and foreground Galactic stars are expected to outnumber field galaxies 7:2 in the low latitude M31 halo field. Color selection appears to retain about two-thirds of all stars in the brightest magnitude bins. This is the expected fraction enclosed within the  $1.5\sigma$  ellipse (see *UBRI* selection criterion in Sec. 3.2) for a two dimensional Gaussian distribution. Morphological selection picks out  $\gtrsim 50\%$  of the remaining objects. This fraction is significantly less than unity (even at bright magnitudes where the effect of galaxy contamination is negligible) because of measurement error in the angular size (due to photon noise, crowding, etc.) coupled with the fact that the PSF quality is not constant over the CCD image. While increasing the value of  $\theta_{\text{crit}}$  would include more stars, it would also correspondingly increase the number of barely resolved galaxies that pass FWHM

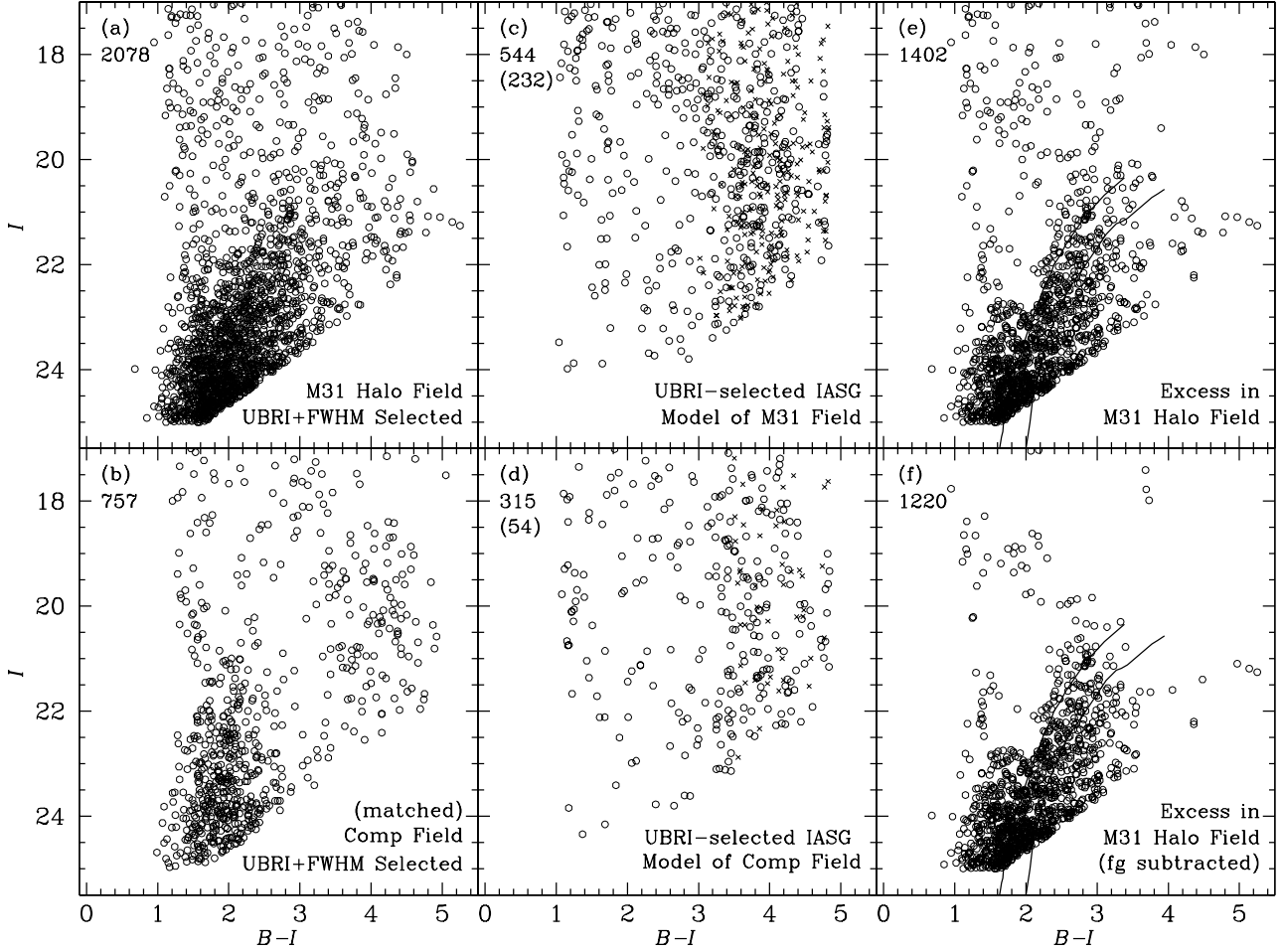


Fig. 8.— Color-magnitude diagrams illustrating the statistical removal of contaminants. The number of objects in each panel is indicated in the upper left. RGB fiducials are the same as in Fig. 6. (a+b) Same as for Fig. 7(e+f). (c+d) CMDs derived from IASG model predictions for the M31 halo and comparison fields, respectively. The faint crosses indicate the fraction of faint red lower main sequence stars that fail the color selection test; their number is given in parentheses. (e) Statistical excess of objects in the M31 halo field CMD in (a) over that in (b). (f) Same as (e) corrected for excess foreground contamination in the M31 halo field [(c) minus (d)].

TABLE 1.  
Fraction of Color and Morphology-selected Objects

$I$	Full Sample	Color Selected	FWHM Selected	Combined Selection	Color/ Full	Combined/ Color	Combined/ Full
M31 Halo Field							
17–18	144	102	75	55	0.71	0.54	0.38
18–19	192	136	89	64	0.71	0.47	0.33
19–20	237	130	104	66	0.55	0.51	0.28
20–21	430	223	176	101	0.52	0.45	0.23
21–22	805	379	314	184	0.47	0.49	0.23
22–23	1384	629	592	333	0.45	0.53	0.24
23–24	2156	992	1069	543	0.46	0.55	0.25
24–25	1996	1052	1103	620	0.53	0.59	0.31
(Matched) Comparison Field							
17–18	64	47	37	30	0.73	0.64	0.47
18–19	109	54	53	33	0.50	0.61	0.30
19–20	211	105	72	50	0.50	0.48	0.24
20–21	298	127	103	65	0.43	0.51	0.22
21–22	488	189	149	75	0.39	0.40	0.15
22–23	837	275	326	116	0.33	0.42	0.14
23–24	1262	373	594	186	0.30	0.50	0.15
24–25	880	287	442	135	0.33	0.47	0.15

selection. Overall the combined selection efficiency for stars at bright magnitudes is  $\sim 30\%$ .

At magnitudes fainter than about  $I = 20$ , the *UBRI* selection step picks only  $\sim 50\%$  of all objects. It should be noted though that this is *not* a direct measure of the star selection efficiency. The measured fraction of selected objects is decreased (relative to the ‘true’ *UBRI* selection efficiency for stars) by the presence of field galaxies in the unselected sample which dominate the sample at the faintest magnitudes. Some of these galaxies happen to have star-like colors, however, and these contaminants tend to increase the color-selected fraction. The increased importance of systematic, non-Gaussian errors at faint magnitudes (e.g. due to interference from close neighbors, sky background measurement error) likely causes more than a third of the stars to escape color selection. FWHM selection at faint magnitudes retains  $\sim 50\%$  of the color-selected subsample, but this is not necessarily a good measure of the morphological selection efficiency for stars for reasons explained above. The true FWHM selection efficiency at faint magnitudes is expected to be lower than  $50\%$  (the estimated efficiency at bright magnitudes) because of increased error in the measurement of  $\theta_{\text{FWHM}}$ . Thus, the overall selection efficiency for faint stars is likely in the range  $10\% - 20\%$ .

The comparison field data are also useful for investigating the selection efficiency. As noted earlier, this field is at a slightly higher Galactic latitude than the M31 halo field and therefore contains a smaller number of foreground Galactic dwarf stars. Thus the star-to-galaxy ratio is lower in the comparison field even for magnitudes brighter than  $I = 20$ , a range in which there is no contribution from M31 red giant stars in the M31 halo field sample. It is therefore no surprise that the fraction of color- and morphology-selected objects is somewhat lower in the comparison field than in the M31 halo field over the full range of apparent brightnesses (Table 1). A more detailed comparison between the selection efficiencies in the M31 halo and comparison fields is precluded by subtle differences in their faint end noise characteristics and in the seeing FWHM (which affect the *UBRI*- and FWHM-selected fractions, respectively).

## 4. Discussion

### 4.1. Estimating the Metallicity of M31’s Outer Spheroid

The metallicity of the population of M31 halo stars detected is estimated by comparing the color-magnitude distribution of the *UBRI*- and FWHM-selected, statistically-subtracted sample of objects to the RGB fiducials for the Galactic globular clusters M5 and 47 Tuc in Fig. 8(f). Clearly the fiducial for M5 is not a good match as most of the M31 halo field objects brighter than  $I = 23$  are redder, and hence more metal rich, than M5

( $[\text{Fe}/\text{H}] = -1.4$ ). The clump of faint ( $I > 23$ ), blue ( $B - I \sim 1 - 2$ ) objects in this plot is produced at least in part by residual contamination by distant faint blue field galaxies [compare Figs. 8(c) and (f)]. The fiducial for 47 Tuc is a better match to the data, and yet there is a substantial spread about this fiducial. A substantial fraction of the objects with  $I < 23$  lie to the right of the 47 Tuc fiducial which indicates that the mean metallicity of M31’s outer halo is comparable to, and possibly a bit higher than, that of 47 Tuc ( $[\text{Fe}/\text{H}] = -0.70$ ), with a fairly large spread in color.

The mean photometric errors estimated from Poisson noise are  $\sigma_{B-I} \simeq 0.02$  for objects near the tip of the M31 RGB ( $I \sim 20.5$ ) and  $\sigma_{B-I} \simeq 0.18$  near the limit of the sample ( $I \sim 24$ ). The observed spread in color is too large to be accounted for simply in terms of photometric error. Despite our efforts to remove all possible contaminants, some of the observed spread could be due to residual contamination from foreground Galactic stars and background faint compact galaxies. The IASG model has not been thoroughly tested at faint magnitudes; moreover, Poisson fluctuations in the field galaxy counts cause differences between the comparison and M31 halo fields. These possible contaminants cannot be entirely responsible for the observed color spread however as there is no reason why the contaminants should contribute primarily near the observed CMD location of the M31 RGB. In fact, compact galaxies contribute primarily at faint magnitudes ( $I \gtrsim 22$ ) and blue colors ( $B - I \leq 2$ ) as can be seen by comparing the *UBRI*- and FWHM-selected comparison field sample in Fig. 8(b) with the IASG model prediction for this field in Fig. 8(d). The uncertainty of the IASG model at faint magnitudes is harder to quantify; some Galactic stars may still be contaminating even the foreground subtracted CMD in Fig. 8(f). We conclude that much of the spread observed in the RGB concentration is due to a true spread in the metallicity of M31 halo stars. Future followup spectroscopy will test this conclusion (Sec. 4.3).

## 4.2. Comparison of this Study to Recent HST Studies

In this section, we compare the final, statistically-subtracted sample of RGB candidates in the M31 halo CMD to those found in the *HST* studies of Holland et al. (1996) and Rich et al. (1996). Fig. 1 shows the locations of all the fields in relation to M31’s disk and halo (schematic representation). We adopt the authors’ plausible hypothesis that the vast majority of objects seen in Rich et al.’s  $R = 40$  kpc (G1) CMD and in Holland et al.’s  $R = 7.6$  kpc (G302) and 10.8 kpc (G312) CMDs are M31 field halo stars (see details below). We use the External Galaxy Model (EGM) developed by Hodder (1995) to estimate the number of halo and disk stars expected to be seen in each of these fields. The EGM is an



adaptation of the Bahcall & Soneira (1984) Galaxy model designed to give star counts and color distributions for any field in an external spiral galaxy using a de Vaucouleurs profile for the halo and an exponential disk.

There is a large number of free parameters in the EGM (disk and halo scale lengths, density ratio, halo axis ratio, and overall normalization), but a plausible model based on 47 Tuc’s red giant luminosity function and color distribution, a disk exponential scale length of 5.5 kpc, a halo effective radius of 2.6 kpc, and an axis ratio for the halo of 0.6 can be normalized to match the star counts observed in the *HST* fields to within  $\sim 3\%$ . Furthermore, the fraction of M31 disk stars predicted by the EGM for the two Holland et al. fields agrees with the upper limits to the fractional disk contamination estimated by the authors: 0.1 for G302 and 0.03 for G312. The halo effective radius of 2.6 kpc for the major axis corresponds to a minor axis effective radius of 1.6 kpc for the flattened halo. This is consistent with the minor axis effective radius of 1.3 kpc found by Pritchett & van den Bergh (1994). The EGM predicts about 6500 RGB stars with  $20 < I < 24$  within the 210 arcmin<sup>2</sup> effective area of the KPNO image of the M31 halo. Most of these are expected to be halo giants with negligible contamination from M31’s disk (0.01%). Table 2 presents the observed number of stars and EGM predictions for this study and for the three *HST* fields.

The surface density of M31 stars predicted by the EGM in the  $R = 19$  kpc field we have studied is lower than in any of the three *HST* fields, even Rich et al.’s G1 field at  $R = 40$  kpc. A 5:3 flattened halo contributes about equally to the G1 field and ours, but M31’s disk contributes an additional 70% (40% of total) in the G1 field. Contrary to the impression one may get from Fig. 1, the degree of disk contamination is much higher in G1 than in the inner Holland et al. (G302) field. Even though the G302 field is expected to contain *more* disk stars than G1, this is more than compensated by the much larger number of halo stars in G302, making the fractional disk contamination in G302 quite small. This is simply a reflection of the fact that galaxy halos have steeper density profiles than the typical disk exponential law. The M31 disk RGB fraction in G1 could be even higher if the halo is less flattened ( $b/a > 0.6$ ) and/or if a thick disk is present. Thus, the large spread in the M31 halo metallicity inferred by Rich et al. may in fact be due primarily to disk contamination (possibly including stars with super-solar [Fe/H]).

After FWHM and *UBRI* selection and statistical subtraction, we detect 665 objects down to a limit of  $I < 24$  in the M31 halo field [see Fig. 8(f)], whereas the EGM predicts about 6500. This would seem to indicate a  $\sim 10\%$  selection efficiency, but the efficiency is higher than this over most of the magnitude range. About  $\sim 30\%$  of the number predicted by the EGM is observed in the range  $20 < I < 22$ , which is close to estimated efficiency

TABLE 2.  
Observed Star Counts and EGM Predictions

Field	Area [arcmin <sup>2</sup> ]	$X^a$ [kpc]	$Y^a$ [kpc]	Observed		EGM Predictions <sup>b</sup>	
				$I=20-22$	$I=22-24$	$I=20-22$	$I=22-24$
This Study	210.0	-1.7	-18.7	122 <sup>c</sup>	543 <sup>c</sup>	421 (421)	6141 (6140)
G302 <sup>d</sup>	3.3	-2.5	-6.7	339	1756	132 (119)	1955 (1748)
G312 <sup>d</sup>	3.3	+0.5	-11.1	82	436	33 (32)	486 (479)
G1 <sup>e</sup>	1.1	+33.6	+4.6	33	140	10 (6)	157 (91)

<sup>a</sup>  $(X, Y)$  = Projected distance of field center from M31’s center along its major and minor axes, respectively

<sup>b</sup> Numbers in parentheses indicate spheroid stars

<sup>c</sup> The star selection efficiency for our  $R = 19$  kpc sample is estimated to be about 30% for the brighter apparent magnitude range and probably as low as 10%–20% for fainter stars

<sup>d</sup> From the study by Holland et al. (1996)

<sup>e</sup> From the study by Rich et al. (1996)

of the star selection process at relatively bright magnitudes (as discussed in Sec. 3.6). At fainter magnitudes the selection efficiency drops for a variety of reasons: non-gaussian photometric errors (effect of crowding on isophotal definition, sky measurement errors, etc.) and increased FWHM measurement error (causing stars to scatter beyond  $\theta_{\text{crit}}$ ). Overall, the number of objects seen in our field is roughly consistent with the EGM model prediction given the selection efficiency.

The estimated metallicity of M31’s outer halo from our study (Sec. 4.1) is consistent with that found in the recent *HST* studies. Holland et al. (1996) find a spread in metallicity of  $-2 \lesssim [\text{Fe}/\text{H}] \lesssim -0.2$  with the majority of stars having  $[\text{Fe}/\text{H}] \simeq -0.6$ . The contamination due to M31 disk stars is estimated using the EGM to be  $\sim 0.1$  for the G302 field and  $\sim 0.03$  for the G312 field. This, along with the estimated foreground Galactic contamination of only 15 disk stars, cannot completely explain the population of very red (high metallicity) objects observed in the G302 and G312 fields. If the disk of M31 is warped, however, the fractional disk contamination could be higher in these Holland et al. fields. Rich et al. (1996) find the field population around G1 to be as metal rich as 47 Tuc, but warn that the apparent high metallicity could also be due to the sample containing objects of intermediate age. As discussed above, contamination by M31’s disk is expected to be significant in the G1 field.

### 4.3. Density and Size of the M31 Halo

The observed RGB counts in the Holland et al. (1996) *HST* minor axis fields and in our  $R = 19$  kpc minor axis field can be used to constrain the physical parameters of M31’s halo. The halo is assumed to be oblate and viewed edge on—i.e., with its symmetry axis in the plane of the sky. A (deprojected) power law index of  $\nu = -3.8$  fits the surface densities observed in the  $R = 7.6$  kpc (G302) and 10.8 kpc (G312) Holland et al. fields derived from stars with  $20 < I < 23.5$ . This slope is a bit shallower than but consistent with the range of  $\nu = -4$  to  $-5$  found by Pritchett & van den Bergh (1994) over the (minor axis) radial range of  $R = 3 - 20$  kpc based on stars within 2 mag of the tip of the RGB. Pritchett & van den Bergh find that M31’s halo density profile steepens with increasing radius (in a log-log plot), so it is not surprising that a single power law fit to the inner halo ( $R < 10.8$  kpc) is shallower than one that includes the outer halo.

For a power law density profile, the column density at a projected radial distance  $R$  along the minor axis is given by:

$$N = \int_{-\infty}^{\infty} n_0 \left[ \frac{x^2 + (R/c)^2}{R_0^2} \right]^{\nu/2} dx \quad (5)$$

$$N = n_0 \left( \frac{R}{c} \right) \left( \frac{R_0 c}{R} \right)^{-\nu} G(\nu) \quad (6)$$

where  $c = 0.6$  is the halo axial ratio,  $x$  is the distance along the line of sight, and

$$G(\nu) \equiv \frac{\Gamma(-\nu/2 - 1/2) \Gamma(1/2)}{\Gamma(-\nu/2)} \quad (7)$$

The volume density  $n_0$ , at a radial distance  $R_0$  in the equatorial plane of the halo, may thus be inferred from the observed surface density:

$$n_0 = \frac{N c}{R G(\nu)} \left( \frac{R}{R_0 c} \right)^{-\nu} \quad (8)$$

The halo volume density is calculated in the apparent magnitude range  $20 < I \leq 23.5$  to avoid red clump stars and to directly compare to Morrison’s (1993) measurement of the local Galactic halo stellar density. A projected density of  $N = 7870 \text{ kpc}^{-2}$  is derived from counts of stars (1290) in this  $I$  magnitude range in the inner Holland et al. field (G302). The area of this field (two Wide Field Camera CCDs) is  $3.3 \text{ arcmin}^2$  which corresponds to  $0.17 \text{ kpc}^2$  at the distance of M31. The inner (7.6 kpc) Holland et al. field, G302, is not exactly on the minor axis; the ellipse with  $c = 0.6$  that intersects this field has a semi-minor axis length of  $R = 6.8 \text{ kpc}$ , and this is the value used in the above equations.

As M31 is about  $\Lambda \approx 1.5$  times larger than the Galaxy, we choose  $R_0 = 12 \text{ kpc}$  in order to calculate the halo density at a position in M31 comparable to the solar location in the Galaxy. The derived M31 halo density at  $R_0 = 12 \text{ kpc}$  is  $n_0 = 341 \text{ kpc}^{-3}$ . Thus,  $n_0$  is much larger than the local Galactic halo density of  $36 \text{ kpc}^{-3}$  for stars with  $M_V \leq 0.5$  (Morrison 1993). This indicates that M31’s halo is much denser, and/or larger than that of the Galaxy,  $(\rho_{\text{M31}}^{\text{RGB}}/\rho_{\text{MW}}^{\text{RGB}})(\Lambda/1.5)^{-\nu} \sim 9.5 \pm 0.3$ , where  $\Lambda$  is the ratio of the characteristic radial scale lengths of M31 and the Galaxy,  $\nu \sim -3.8$  is the power law density profile slope, and the (formal) error bar is based on Poisson error in the star counts in the inner Holland et al. field, G302. The uncertainty in the overdensity estimate is substantially higher than the formal error bar quoted above when one takes into account the possible range of profile slopes,  $\nu$  (see below).

The actual density of M31’s inner halo is likely to be even higher than this estimate: We have adopted a single power law profile in the above integral, with a slope of  $\nu = -3.8$

based on M31’s inner halo, but the outer profile is known to steepen both from the counts in our  $R = 19$  kpc field and from Pritchett & van den Bergh (1994); this leads to an overestimate of the column density for a given spatial density  $n_0$ , or to an underestimate of  $n_0$  since we normalize to the *observed* column density. At any rate, it is clear that the halo of M31 is significantly denser/larger than the halo of the Galaxy.

The density profile of the outer halo of M31 (beyond a minor axis radius of 10 kpc) has a slope of  $\nu \approx -5$ , as indicated by the EGM de Vaucouleurs spheroid fit to the observed counts at  $R = 10.8$  kpc (G312, Holland et al. 1996) and  $R = 19$  kpc (this study), and by Pritchett & van den Bergh’s (1994) study. This is steeper than the profile of outer Galactic halo which may be approximated by a power law index in the range  $\nu_{\text{MW}} = -3.0$  to  $-3.5$  (Zinn 1985; Preston et al. 1991; Gould et al. 1998). There are significant uncertainties though in these measurements of the profile of the Galaxy’s outer stellar halo, and the halo of M31 is not well fit by a power law but rather by a de Vaucouleurs law (Pritchett & van den Bergh 1994), so directly comparing the power law indices may be misleading.

#### 4.4. Future Work/Followup Spectroscopy

Although it is becoming increasingly clear that the halo of M31 is fairly metal rich, an accurate mean metallicity and spread remain to be determined. Contamination from foreground Galactic stars and background field galaxies, as well as from disk RGB stars in M31, is still non-negligible. The combined color- and morphological-selection technique described in this paper can be used effectively to study M31’s inner halo where the fractional contamination is expected to be lower than in our  $R = 19$  kpc field. High angular resolution imaging (e.g., with *HST*) can help reduce background galaxy contamination.

We are currently undertaking followup Keck/LRIS spectroscopy of the brightest decade of M31 halo RGB candidates in the *UBRI*- and FWHM-selected sample [Fig. 6(d)] (Guhathakurta & Reitzel 1998). Candidates for spectroscopic observation are selected without regard to color, so as not to introduce any metallicity bias. We do not select objects from the statistically-subtracted version of the CMD as it is not complete. Spectroscopy should allow kinematic confirmation of the identity of M31 RGB stars: galaxies are eliminated altogether on the basis of their redshift and M31 stars are quite well separated from foreground Galactic disk stars ( $v_{\text{M31}}^{\text{sys}} \sim -300$  km s<sup>-1</sup> vs  $v_{\text{MW disk}} \approx 0$  km s<sup>-1</sup>). A broad versus narrow distribution of radial velocities will distinguish M31 halo stars from disk stars on M31’s minor axis, respectively. In addition to removal of residual contaminants, spectroscopy allows a direct measurement of the metallicity of each star using the near infrared Ca II line strengths,  $W_{\text{Ca}}$ . A well developed empirical calibration method exists

to determine  $[\text{Fe}/\text{H}]$  from  $W_{\text{Ca}}$  and the brightness of the star  $\delta I$  relative to the horizontal branch level (Olszewski et al. 1991; Armandroff & Da Costa 1991; Suntzeff & Kraft 1996).

## 5. Summary

We analyze deep *UBRI* images obtained with the KPNO 4-meter telescope of a field in the outer halo of M31 ( $R = 19$  kpc in projection on the minor axis of M31), and of a comparison field located at similar Galactic coordinates. Keck/LRIS *I* band images of the M31 halo field are used for the purpose of making angular size measurements and morphological star-galaxy separation. We use a *UBRI* color selection technique in conjunction with morphological selection to isolate a sample of M31 RGB stars from the numerous background population of faint field galaxies. A detailed comparison shows that the M31 halo field contains an excess of objects over the populations present in the comparison field. An empirical Galactic (IASG) model is used to estimate the foreground contamination from Galactic stars in both fields; the predicted number of bright stars agrees well with the observed distributions in the M31 halo field and the comparison field. We use the comparison field data and the IASG model to statistically subtract contaminants from the M31 halo field, revealing a distribution of objects at the expected location of the RGB at the distance of M31. These stars have a mean metallicity of  $[\text{Fe}/\text{H}] \geq -0.7$  with a significant spread about this value, ranging from M5 ( $[\text{Fe}/\text{H}] = -1.4$ ) to more metal rich than 47 Tuc ( $[\text{Fe}/\text{H}] = -0.70$ ). This result is in good agreement with recent *HST* studies of the halo of M31 by Holland et al. (1996) and Rich et al. (1996). The spatial density of M31’s halo red giants is an order of magnitude greater than the red giant density at a comparable radius in the Milky Way halo. Alternatively, the halo of M31 has a characteristic size scale almost 3 times larger than that of the Galactic halo. The outer stellar halo of M31 has a steeper slope ( $\nu \sim -5$ ) than that of the Galaxy ( $\nu = -3$  to  $-3.5$ ).

The early phases of this research were supported by a CalSpace grant and a Divisional Seed grant at UC Santa Cruz. A. G. was supported in part by NSF grant AST 9420746 and in part by NASA grant NAG 5-3111. We would like to thank the anonymous referee for helpful suggestions that have led to an improvement of the paper. Some of the data presented herein were obtained at Kitt Peak National Observatory, which is operated by Association of Universities for Research in Astronomy, Inc., while some of the data were obtained at the W. M. Keck Observatory, which is operated as a scientific partnership among the California Institute of Technology, the University of California, and the National Aeronautics and Space Administration. The W. M. Keck Observatory was made possible

by the generous financial support of the W. M. Keck Foundation.

## REFERENCES

- Armandroff, T. E. & Da Costa, G. S. 1991, *AJ*, 101, 1329
- Bahcall, J. N., & Soneira, R. M. 1984, *ApJS*, 55, 67
- Bertelli, G., Bressan, A., Chiosi, C., Fagotto, F., & Nasi, E. 1994, *A&AS*, 106, 275
- Burstein, D., & Heiles, C. 1982, *ApJS*, 54, 33
- Cardelli, J. A., Clayton, G. C., & Mathis, J. S. 1989, *ApJ*, 345, 245
- Carney, B. W., Aguilar, L., Latham D. W., & Laird J. B. 1990, *AJ*, 99, 201
- Christian, C. A., & Heasley, J. N. 1991, *AJ*, 101, 848
- Couture, J., Racine, R., Harris, W. E., & Holland, S. 1995, *AJ*, 109, 2050
- Crotts, A. P. S. 1986, *AJ*, 92, 292
- Davidge, T. J. 1993, *ApJ*, 409, 190
- de Vaucouleurs, G. 1958, *ApJ*, 128, 465
- Durrell, P. R., Harris, W. E., & Pritchett, C. J. 1994, *AJ*, 108, 2114
- Eggen, O. J., Lynden-Bell, D., & Sandage, A. R. 1962, *ApJ*, 136, 748
- Freedman, W. F., & Madore, B. F. 1990, *ApJ*, 365, 186
- Gould, A., Bahcall, J. N., & Flynn, C. 1996, *ApJ*, 465, 759
- Gould, A., Bahcall, J. N., & Flynn, C. 1997, *ApJ*, 482, 913
- Gould, A., Flynn, C., & Bahcall, J. N. 1998, *ApJ*, in press (astro-ph 9711263)
- Gould, A., Guhathakurta, P., Richstone, D., & Flynn, C. 1992, *ApJ*, 388, 345 (GGRF)
- Green, E. M., Demarque, P., & King, C. R. 1987, *The Revised Yale Isochrones and Luminosity Functions* (New Haven: Yale University Observatory)
- Guhathakurta, P., & Reitzel, D. B. 1998, *ApJL*, in preparation
- Hodder, P. J. C. 1995, Ph.D. thesis, University of British Columbia
- Holland, S., Fahlman, G. G., & Richer, H. B. 1996, *AJ*, 112, 1035
- Holtzman, J. A., Burrows, C. J., Casertano, S., Hester, J. J., Trauger, J. T., Watson, A. M., & Worthey, G. 1995, *PASP*, 107, 1065

- Huchra, J. P., Brodie, J. P., & Kent, S. M. 1991, *ApJ*, 370, 495
- Jarvis, J. F., & Tyson, J. A. 1981, *AJ*, 86, 476
- Landolt, A. U. 1983, *AJ*, 88, 439
- Larson, R. B. 1974, *MNRAS*, 166, 585
- Lilly, S. J., Hammer, F., Le Fèvre, O., & Crampton, D. 1995a, *ApJ*, 455, 75
- Lilly, S. J., Le Fèvre, O., Crampton, D., Hammer, F., & Tresse, L. 1995b, *ApJ*, 455, 50
- Morrison, H. L. 1993, *AJ*, 106, 578
- Mould, J. 1986, in *Stellar Populations*, edited by C. Norman, A. Renzini, and M. Tosi (Cambridge: Cambridge University Press), p. 9
- Mould, J., & Kristian, J. 1986, *ApJ*, 305, 59
- Oke, J. B., Cohen, J. G., Carr, M., Cromer, J., Dingizian, A., Harris, F. H., Labrecque, S., Lucinio, R., Schall, W., Epps H., & Miller, J. 1995, *PASP*, 107, 375
- Olszewski, E. W., Schommer, R. A., Suntzeff, N. B., & Harris, H. C. 1991, *AJ*, 101, 515
- Preston, G. W., Sheckman, S. A., & Beers, T. C. 1991, *ApJ*, 375, 121
- Pritchett, C. J., & van den Bergh, S. 1988, *ApJ*, 331, 135
- Pritchett, C. J., & van den Bergh, S. 1994, *AJ*, 107, 1730
- Ratnatunga, K. U., & Bahcall, J. N. 1985, *ApJS*, 59, 63
- Reitzel, D. B., Guhathakurta, P., & Gould, A. 1996a, in *Formation of the Galactic Halo....Inside and Out*, edited by H. Morrison and A. Sarajedini (ASP Conf. Series, No. 92), p. 540
- Reitzel, D., Guhathakurta, P., & Gould, A. 1996b, in *New Light on Galaxy Evolution*, edited by R. Bender and R. L. Davies (Kluwer, Dordrecht), p. 437
- Rich, R. M., Mighell, K. J., Freedman, W. L., & Neill, J. D. 1996, *AJ*, 111, 768
- Searle, L., & Zinn, R. 1978, *ApJ*, 225, 357
- Stetson, P. B. 1987, *PASP*, 99, 191
- Stetson, P. B. 1992, in *Astronomical Data Analysis Software*, edited by D. M. Worrall, C. Biemesderfer, and J. Barnes (ASP Conf. Series, No. 25), p. 297
- Suntzeff, N. B., & Kraft, R. P. 1996, *AJ*, 111, 1913
- Valdes, F. 1982, *SPIE*, 331, 465
- Williams, R. E., Blacker, B., Dickinson, M., Dixon, W. V., Ferguson, H. C., Fruchter, A. S., Giavalisco, M., Gilliland, R. L., Heyer, I., Katsanis, R., Levay, Z., Lucas, R. A., McElroy, D. B., Petro, L., & Postman, M. 1996, *AJ*, 112, 1335



Zinn, R. 1985, ApJ, 293, 424

Zinn, R. 1993, in *The Globular Cluster-Galaxy Connection*, edited by G. H. Smith and J. P. Brodie (ASP Conf. Series, No. 48), p. 38